

Comparison between Eulerian diagnostics and finite-size Lyapunov exponents computed from altimetry in the Algerian basin

F. d'Ovidio ^{a,*}

Jordi Isern-Fontanet ^{b,c}

Cristóbal López ^d

Emilio Hernández-García ^d

Emilio García-Ladona ^e

^a*Laboratoire d'Océanographie et du Climat: Expérimentation et Approches Numériques, IPSL, Paris, France and Institute of Complex Systems, Paris Ile-de-France (ISC-PIF)*

^b*Laboratoire de Physique des Océans, Ifremer, Plouzané, France.*

^c*Laboratoire d'Océanographie Spatiale, Ifremer, Plouzané, France.*

^d*Instituto de Física Interdisciplinar y Sistemas Complejos IFISC (CSIC-UIB), Campus Universitat de les Illes Balears, E-07122 Palma de Mallorca, Spain.*

^e*Institut de Ciències del Mar, Passeig Marítim de la Barceloneta 37-43, E-08003 Barcelona, Spain.*

Abstract

Transport and mixing properties of surface currents can be detected from altimetric data by both Eulerian and Lagrangian diagnostics. In contrast with Eulerian diagnostics, Lagrangian tools like the local Lyapunov exponents have the advantage of exploiting both spatial and temporal variability of the velocity field and are in principle able to unveil subgrid filaments generated by chaotic stirring. However, one may wonder whether this theoretical advantage is of practical interest in real-data, mesoscale and submesoscale analysis, because of the uncertainties and resolution of altimetric products, and the non-passive nature of biogeochemical tracers. Here we compare the ability of standard Eulerian diagnostics and the finite-size Lyapunov exponent in detecting instantaneous and climatological transport and mixing properties. By comparing with sea-surface temperature patterns, we find that the two diagnostics provide similar results for slowly evolving eddies like the first Alboran gyre. However, the Lyapunov exponent is also able to predict the (sub-)mesoscale filamentary process occurring along the Algerian current and above the Balearic Abyssal Plain. Such filaments are also observed, with some mismatch, in sea-surface temperature patterns. Climatologies of Lyapunov exponents do not show any compact relation with other Eulerian diagnostics, unveiling a different

structure even at the basin scale. We conclude that filamentation dynamics can be detected by reprocessing available altimetric data with Lagrangian tools, giving insight into (sub-)mesoscale stirring processes relevant to tracer observations and complementing traditional Eulerian diagnostics.

Key words: Submesoscale, filaments, altimetry, Mediterranean circulation, Lagrangian dynamics

1 Introduction

2 Satellite high-resolution daily images of tracers like sea-surface temperature and chloro-
3 phyll show a large mesoscale and sub-mesoscale heterogeneity and patchiness, typically
4 in the form of filaments. The full range of tracer variability observed in a climatologi-
5 cal mean at the basin scale, can occur in daily snapshots over spatial scales of just 10-
6 100 km (see for instance Lehahn et al. (2007) for the case of chlorophyll in the NE At-
7 lantic). This large heterogeneity occurring on relatively short distances is able to induce
8 very strong tracer gradients and to impact on important aspects of the ocean dynamics like
9 lateral transport, upwelling/downwelling, and mixing. Mesoscale and sub-mesoscale variabil-
10 ity is an important component of plankton dynamics (Abraham, 1998; López et al., 2001;
11 Abraham et al., 2000; Boyd et al., 2000; Toner et al., 2003; Martin, 2003), larval transport
12 (Bradbury and Snelgrove, 2001), as well as the dispersion of contaminants and oil spills. In
13 polar regions, (sub-)mesoscale tracer variability has been recently recognised to impact also
14 on the thermohaline properties of the mixed layer, affecting the low frequency ocean cir-
15 culation through the formation of waters below the mixed layer (Sallee et al., 2006, 2007).
16 Mesoscale and sub-mesoscale gradients of heat and salinity can induce cells of very strong
17 vertical velocities (several tens of meters per day) from subsurface down to and below
18 the mixed layer depth. These vertical velocities may fertilise the photic layer, creating lo-
19 cal plankton blooms and affecting the sequestration of organic matter from the surface
20 (Lévy et al., 2001, 2005). This mechanism can affect the properties of deep waters when
21 they are formed (Paci et al., 2005). Tracer gradient intensification is also a precondition to
22 mixing. Horizontally, the elongation of water masses in thin structures intensifies local gradi-
23 ents, greatly enhancing background diffusion (Lapeyre et al., 2006). Vertically, the trapping
24 of inertial waves inside filaments creates mixing hotspots that extends to the bottom and
25 below the mixed layer depth (Young et al., 1982).

26 Tracer mesoscale and sub-mesoscale patches are often found associated to surface mesoscale
27 eddies (e.g. Robinson, A. R. et al. (1993); McGillicuddy et al. (1998); Martin et al. (2002);
28 Abraham and Bowen (2002); Morrow et al. (2004); Legal et al. (2006)). Tracers are stretched
29 into filaments by the shear-dominated regions in between mesoscale eddies while the recir-
30 culating regions inside eddies' cores can trap and transport tracer anomalies for timescales

* Corresponding author.

Email addresses: dovidio@lmd.ens.fr (F. d'Ovidio), jisern@ifremer.fr
(Jordi Isern-Fontanet), clopez@ifisc.uib.es (Cristóbal López),
emilio@ifisc.uib.es (Emilio Hernández-García), emilio@cmima.csic.es
(Emilio García-Ladona).

31 comparable to the eddy lifetime. As a well-known tool to reveal geostrophic velocities asso-
32 ciated to eddies, altimetry data when opportunely analyzed, provide an important source of
33 information for the mesoscale and sub-mesoscale structuration of tracer distributions.

34 Traditionally, transport information has been inferred from altimetry with Eulerian diag-
35 nostics like the eddy kinetic energy, the Okubo-Weiss criterion that separates the eddy's core
36 from the periphery and others, that will be discussed in detail shortly. These diagnostics are
37 based on the analysis of instantaneous snapshots of tracer and velocity fields. For instance,
38 the Okubo-Weiss (OW) parameter has been applied to drifters in order to characterize
39 eddy properties (Stocker and Imberger, 2003; Testor and Gascard, 2005), to in situ density
40 profiles to identify regions with different mixing properties (Isern-Fontanet et al., 2004),
41 and to altimetric maps with similar objectives (Isern-Fontanet et al., 2004; Waugh et al.,
42 2006). The OW parameter has also widely been used for the identification and charac-
43 terization of ocean eddies from altimetry (Isern-Fontanet et al., 2003; Morrow et al., 2004;
44 Chaigneau and Pizarro, 2005; Isern-Fontanet et al., 2006). More recently, it has been sug-
45 gested that Lagrangian diagnostics are more appropriate to link turbulence properties to
46 tracer dynamics. The most used Lagrangian diagnostics have been the calculation of local
47 Lyapunov exponents, that measure the relative dispersion of advected particles. In contrast
48 to Eulerian tools, Lagrangian diagnostics do not analyze instantaneous snapshots of the
49 velocity field, but measure transport properties along particle trajectories, therefore recon-
50 structing the fine structure of transport dynamics that a fluid parcel has experienced, like
51 subgrid filament formation. These patterns depend on the advection history along a tra-
52 jectory, that may span a large spatiotemporal domain of the velocity field, and therefore
53 cannot be captured by Eulerian diagnostics, that instead measure local, properties. Regard-
54 ing Lagrangian tools like the finite-size or finite-time Lyapunov exponents (resp. FSLEs and
55 FTLEs) Abraham and Bowen (2002) computed FTLEs from time-dependent velocity fields
56 and compared to instantaneous SST patterns, LaCasce and Ohlmann (2003) used FSLEs
57 to study the statistics of a large data set of drifting buoys; Waugh et al. (2006) applied
58 FTLEs to altimetry and compared the results with OW and kinetic energy estimations;
59 Lehahn et al. (2007) computed FSLEs from the geostrophic field in order to extract trans-
60 port barriers and compared with satellite derived plankton and SST patches; Rossi et al.
61 (2008) compared mixing and productivity by using the FSLE. Besides these studies, the
62 FSLE has been also applied to numerical simulations of the Mediterranean sea with different
63 objectives: the predictability of Lagrangian trajectories (Iudicone et al., 2002) and the char-
64 acterization of flow patterns (d'Ovidio et al., 2004) and dispersion (García-Olivares et al.,
65 2005).

66 However, for the case of real velocity data and given the chaotic nature of mesoscale advec-
67 tion (in the sense of positive Lyapunov exponents) one may expect Lagrangian diagnostics
68 to be more affected than Eulerian tools by any space and time indetermination of the ve-
69 locity field. When dealing with real altimetric data, therefore one may ask whether the
70 theoretical advantage of Lagrangian techniques of detecting small scale transport structure
71 is not countered in practice by the intrinsic error and cutoff of altimetric data, so that this
72 information is either unreliable or already contained in Eulerian quantities. This question
73 is particularly relevant given the larger computational costs (a few orders of magnitude)
74 of Lagrangian tools in respect to Eulerian ones. In fact, for the case of the Tasman sea
75 Waugh et al. (2006) found a striking resemblance between maps of Lyapunov exponents
76 and the eddy kinetic energy, as well as a compact relationship between the two quantities.
77 In their concluding remarks, Waugh et al. (2006) argued that this observation, if valid in
78 other oceanic basins as well, would rise the possibility of using the EKE for estimating
79 stirring rates, without the need of explicit, longer Lagrangian calculations. However, one
80 of the main advantages of the Lagrangian techniques is the possibility of reconstructing
81 tracer patterns that are below the resolution of the velocity field and that arise due to
82 several iterations of stretching and folding during the tracer (chaotic) advection. Indeed, in

83 Waugh et al. (2006) the correlation between the Lyapunov exponents have been found on a
84 grid at relatively low resolution (0.5 deg.) and for a advection times of 14 days (two altimet-
85 ric images), i.e. without the spatial and temporal information needed for the developement
86 of filaments. Does this result hold also for filament-resolving Lagrangian calculations?

87 In this paper we address this question, exploring the possibility of obtaining reliable in-
88 formation with Lyapunov exponents that is not already contained in Eulerian diagnostics,
89 focusing on filament dynamics.

90 This will be done both on the analysis of individual patterns (validated by high resolution
91 SST images) and on a climatological basis. We find that at (sub-)mesoscale resolution the
92 information provided by Eulerian diagnostics and Lyapunov exponents coincides only for
93 very stationary eddies, while providing two distinct and complementary pictures of the
94 circulation in all the other cases: the Eulerian analysis provides the eddies that populate
95 the mesoscale, while the Lagrangian analysis yields the tracer filaments generated by the
96 spatiotemporal variability of these eddies. Our results also show a surprising reliability of
97 altimetric data at the scale of their nominal resolution, when reprocessed with Lagrangian
98 tools.

99 We will compare Eulerian diagnostics and Lyapunov exponents in the Algerian basin because
100 of its rich and variable mesoscale activity, that contains jet-dominated regions (the path of
101 the Algerian current) as well as eddies with very different characteristics (from the quasi-
102 stationary Alboran gyres, to the slowly propagating eddies of the Balearic Abyssal plain,
103 and the fast-evolving Algerian eddies). A main characteristic of the surface circulation in
104 the Mediterranean sea is the propagation of fresh waters incoming from the Atlantic ocean.
105 At the entrance of the Mediterranean, these waters flow from west to east and form patterns
106 such as the Alboran eddies east of the Gibraltar strait or the Algerian current along the
107 Algerian coast. The instabilities of this current generates, a few times per year, coastal
108 eddies that propagate downstream, usually until the entrance of the Sardinia channel. There,
109 they can detach from the coast and propagate as open sea eddies (Millot, 1999) following
110 relatively well defined paths (Isern-Fontanet et al., 2006). These eddies, called Algerian
111 eddies, have variable diameters of about 50 – 200 *km*, vertical extents from hundreds to
112 thousands of meters, and lifetimes of several months, up to nearly 3 *years* (Millot et al.,
113 1997; Puillat et al., 2002). Their presence has a large impact on the redistribution of tracers
114 in the Algerian basin, which is characterized by the northward spreading of tracers that are
115 initially transported eastwards by the Algerian current (Ovchinnikov, 1966; Brasseur et al.,
116 1996). As we shall see, our analysis of stirring will unveil the crucial role on tracer patterns
117 of the time variability of the mesoscale activity in the Algerian basin and the relevance of
118 topography in constraining the dynamics of coherent structures.

119 The paper is organized as follows. After describing the data sets and the techniques, we de-
120 velop an Eulerian and Lagrangian analysis for specific days. We focus on the representation
121 of eddies and the detection of transport barriers and we get two complementary pictures:
122 a regular and smooth OW-based description and a more complex, lobular representation
123 from the FSLE. We then compare such different structures to tracer distributions. In order
124 to filter out the active dynamics of a real tracer as well as the unresolved components and
125 indeterminacies of altimetry data, we first consider the filaments of a synthetic tracer, that
126 we advect numerically with the altimetric data. As a second step, we take sea-surface tem-
127 perature (SST) satellite images. The indications that are found on the individual days are
128 then generalized in a climatological comparison, where we compare the spatial variability
129 of FSLE, OW parameter, strain rate, and eddy kinetic energy temporally averaged over
130 the period 1994-2004. For both the Eulerian and the Lagrangian analysis, we also propose
131 to describe the consequences of filament formation with a climatology giving the spatial
132 density of transport barriers.

133 **2 Methods**

134 A traditional approach to the characterization of the stirring and mixing in the presence of
 135 mesoscale eddies consists in separating the stagnation region at the eddy’s core from the
 136 eddy’s periphery where tracer filamentation occurs. This is done by measuring the relative
 137 dominance of vorticity and deformation. One of the most used parameters for measuring this
 138 relative dominance is the Okubo-Weiss parameter (Okubo, 1970; Weiss, 1991) which has
 139 been already used by some of us to study properties of Algerian eddies (Isern-Fontanet et al.,
 140 2004). The OW parameter is a particular case of the more general vortex-identification
 141 criterion proposed by Jeong and Hussain (1995).

142 The Okubo-Weiss parameter W is defined as:

143
$$W = s_n^2 + s_s^2 - \omega^2 \tag{1}$$

144 where s_n , s_s and ω are the normal and the shear components of strain, and the relative
 145 vorticity of the flow defined, respectively, by

146
$$s_n = \frac{\partial u}{\partial x} - \frac{\partial v}{\partial y}, \quad s_s = \frac{\partial v}{\partial x} + \frac{\partial u}{\partial y}, \quad \omega = \frac{\partial v}{\partial x} - \frac{\partial u}{\partial y}.$$

147 In the formula above, x and y are orthogonal spatial coordinates and u and v are the
 148 component of the velocity respectively for the x and y directions.

149 The parameter W , allows to separate a two-dimensional flow into different regions: a
 150 vorticity-dominated region ($W < -W_0$), a strain-dominated region ($W > W_0$) and a
 151 background field with small positive and negative values of W ($|W| \leq W_0$). Here $W_0 =$
 152 $0.2\sigma_W$, σ_W being the standard deviation of the W values in the whole domain, in our
 153 case the Mediterranean sea (Bracco et al., 2000; Pasquero et al., 2001; Isern-Fontanet et al.,
 154 2006; Elhmaïdi et al., 1993). The core edge can then be identified as the closed lines with
 155 $W = 0$. This separation of the field in terms of the sign of W has been proved to be a
 156 robust criterion for extracting eddy cores from complex fluid flows (Jeong and Hussain,
 157 1995; Pasquero et al., 2001). In steady flows, the boundary of the core constitutes a bar-
 158 rier to the exchange of particles with the surrounding cell, so that particles trapped in-
 159 side the eddy core remain there. Under non-steady flows, particles can leak out of the
 160 vortices, be ejected through filamentation processes, or even the eddy can be destroyed
 161 (Basdevant and Philipovitch, 1994; Hua and Klein, 1998).

162 The OW parameter has some well-known limitations. On one side, it assumes that velocity
 163 gradients are slowly evolving in time, which is only valid inside relatively coherent regions.
 164 On the other side, this parameter fails to properly identify regions with different mixing
 165 properties when eddies are stationary and have axial symmetry (Lapeyre et al., 1999). There
 166 have been some attempts to solve some of these limitations by extending it to consider the
 167 time evolution of velocity gradients (Hua and Klein, 1998; Hua et al., 1998; Lapeyre et al.,
 168 1999).

169 Another approach to the characterization of flow structures is to assume a Lagrangian
 170 viewpoint, that is, to look explicitly at transport properties from the analysis of particle
 171 trajectories (Pierrehumbert, 1991; Ridderinkhof and Zimmerman, 1992; Miller et al., 1997;
 172 Haller and Yuan, 2000; Coulliette and Wiggins, 2001; Koh and Legras, 2002; d’Ovidio et al.,
 173 2004; Shadden et al., 2005; Mancho et al., 2006). In contrast to the OW method and in

174 general to Eulerian diagnostics, this approach requires knowledge of the time variability of
 175 the velocity field, as well as the use of an integrator for generating the trajectories. Sev-
 176 eral methods exist, one of the simplest being the Finite-Size Lyapunov Exponent (FSLE).
 177 The FSLE is a generalization of the concept of Lyapunov exponent to finite separations.
 178 The standard definition of Lyapunov exponent refers to the exponential rate of divergence,
 179 averaged over infinite time, of infinitesimally closed initial points. The FSLE technique
 180 keeps the original idea of capturing the rate of divergence between trajectories, but over-
 181 comes the limit operations. Thus, it is (and has been shown to be) rather appropriate
 182 to manage real data. The FSLEs were introduced for turbulent flows (Aurell et al., 1997;
 183 Artale et al., 1997) aiming at studying non-asymptotic dispersion processes. Since then,
 184 they have been used for two complementary goals: for characterizing dispersion processes
 185 (Lacorata et al., 2001), and for detecting and visualizing Lagrangian structures (e.g. trans-
 186 port barriers and fronts) (Boffetta et al., 2001; Koh and Legras, 2002; Joseph and Legras,
 187 2002; d’Ovidio et al., 2004). In the framework of this paper, in order to compare with the
 188 OW parameter we will focus mainly on the second use.

189 Several methods allow to calculate the FSLEs. In the simplest scheme, for each instant t
 190 and each point \mathbf{x} , one follows in time the evolution of a tracer started in \mathbf{x} and of another
 191 probing tracer located at a distance δ_0 from it. The integration is stopped when the two
 192 tracers have reached a final separation $\delta_f > \delta_0$. From the time interval, τ , to reach the final
 193 separation, the FSLE is defined in the following way:

$$194 \quad \lambda(\mathbf{x}, t, \delta_0, \delta_f) = \frac{1}{\tau} \log \frac{\delta_f}{\delta_0}. \quad (2)$$

195 In order to reduce the dependence on the direction of the probing tracer, the algorithm is run
 196 choosing three points forming an equilateral triangle around \mathbf{x} . We stopped the integration
 197 when any of these three points reaches a separation δ_f from the trajectory started in \mathbf{x} .

198 Maxima (ridges) of Lyapunov values are typically organized in convoluted, lobular lines. For
 199 the case of the backward calculations, these lines can be interpreted as the fronts of passively
 200 advected tracers. This interpretation can be understood in a very qualitative but effective
 201 way, considering that fronts typically separate fluid patches of different origins. Therefore,
 202 the separation in the past of a couple of points is largest when the couple is initialised
 203 exactly over the front. This argument can be rephrased in a slightly more rigorous way in
 204 the context of dynamical systems, interpreting the line-shaped regions of fastest separa-
 205 tion -either backward or forward in time- respectively as the unstable and stable manifolds
 206 of the hyperbolic points in the flow (Haller and Yuan, 2000; Boffetta et al., 2001; Haller,
 207 2001; Koh and Legras, 2002; Joseph and Legras, 2002; d’Ovidio et al., 2004; Mancho et al.,
 208 2006). The effect on advection of hyperbolic structures is sketched in Fig. 1. Due to the con-
 209 vergent field along the stable manifold and the divergent field along the unstable manifold,
 210 a passively advected tracer is deformed as in Fig. 1, developing a front along the unstable
 211 manifold and a gradient orthogonally to it. Due to the hyperbolic structure of which the
 212 manifold is a part, the tracer front approaches the manifold exponentially fast. The dis-
 213 tance δ_r between the tracer front and the manifold depends on the initial front-to-manifold
 214 distance δ_i , the exponent λ of the manifold, and the time of integration t :

$$215 \quad \delta_r \approx \delta_i \exp(-\lambda t). \quad (3)$$

216 Manifolds characterized by higher exponents have therefore a stronger effect on tracers,
 217 shaping a front in shorter times and being more visible in tracer distributions.

218 Note that for a time-dependent velocity field, the sketch of Fig. 1 holds only if the hyperbolic
219 structures evolve in time on a time scale slower than the tracer advection, so that the tracer
220 can actually relax over the manifold. See Lehahn et al. (2007) for more details on the FSLE
221 computation from altimetric data.

222 Mixing properties can also be diagnosed by Lyapunov exponent calculations, either con-
223 sidering the exponential separation in the future as a measure of tracer dispersion, or by
224 combining forward and backward information (d’Ovidio et al., 2004). Since in this work we
225 aim at a direct comparison with advected tracers (SST), we will focus on the backward
226 calculation and compare the location of the manifolds detected by the FSLEs with tracer
227 fronts.

228 As it is clear from Eq.(2), the FSLEs depend critically on the choice of two length scales:
229 the initial separation δ_0 and the final one δ_f . d’Ovidio et al. (2004) argued that δ_0 has
230 to be close to the intergrid spacing Δx among the points \mathbf{x} on which the FSLEs will be
231 computed. In fact, a δ_0 larger than intergrid spacing would allow to sample manifolds of
232 strong Lyapunov exponents in more than one grid points, while δ_0 smaller than the intergrid
233 spacing would not allow to follow a manifold on the sampling grid as a continuous line.
234 Following d’Ovidio et al. (2004); Lehahn et al. (2007), in this work we have set $\delta_0 = 0.01^\circ$
235 (approx. 1 km) in order to match the resolution of SST images. We have set $\delta_f = 1^\circ$ i.e.,
236 separations of about 110 Km, that is the order of magnitude of the eddies’ radii detected
237 by altimetry. Values of δ_f smaller or larger up to 50% do not change significantly the
238 calculation. The time of integration for finite-size Lyapunov exponents varies from one
239 point of another, being small for strong values and vice versa. Inverting Eq.2,

$$240 \quad \tau = \frac{1}{\lambda} \log \frac{\delta_f}{\delta_0}. \quad (4)$$

241 We found typical values of finite-size Lyapunov exponents in the range $0.1 - 0.2 \text{ days}^{-1}$,
242 corresponding to integration times of resp. 46 and 23 days.

243 3 Data

244 3.1 Sea-Surface Height

245 In the Mediterranean sea, despite the weak signal intensity and the coarse space and time
246 resolution of the altimetric tracks, several studies have shown the reliability of the alti-
247 metric data to analyze its dynamics, particularly in the Algerian basin (Vignudelli, 1997;
248 Bouzinac et al., 1998; Larnicol et al., 2002; Font et al., 2004). In this study we have used
249 Delayed Time Maps of Absolute Dynamic Heights (DT-MADT) produced by *Collecte Local-*
250 *isation Satellites (CLS)* in Toulouse (France) specifically for the Mediterranean sea, which
251 combine the signals of *ERS-ENVISAT* and *TOPEX/Poseidon-JASON* altimeters.

252 Altimetric data are processed including usual corrections (sea-state bias, tides, inverse
253 barometer, etc.) and improved orbits. From several corrected sea-surface height files, a
254 conventional repeat-track analysis is performed to extract the Sea Level Anomaly (SLA)
255 relative to a mean profile: data are re-sampled along the mean profile using cubic splines
256 and differences relative to the mean profile are calculated. SLA along-track data are then

257 filtered and subsampled. The filters used are a non linear median over 3 points (roughly 21
 258 km) followed by a low pass along track linear Lanczos filter (with a cut-off wavelength of 42
 259 km). SLA data are then subsampled every other point (SSALTO/DUACS User Handbook,
 260 2006). Finally, SLA maps are built using an improved space/time objective analysis method,
 261 which takes into account long wavelength errors, on a regular grid (Le Traon et al., 1998) of
 262 $(1/8)^o \times (1/8)^o$ every week. Then, Sea-Surface Heights (SSH) are finally obtained by adding
 263 to the SLA a Mean Dynamic Topography (Rio et al., 2007).

264 For each data set geostrophic velocities are estimated as usual:

$$265 \quad u = -\frac{g}{fR_T} \frac{\partial h_{ssh}}{\partial \phi}, \quad v = \frac{g}{fR_T \cos \phi} \frac{\partial h_{ssh}}{\partial \lambda}, \quad (5)$$

266 where h_{ssh} is the SSH, g is gravity, f the Coriolis parameter, R_T the Earth radius, ϕ the
 267 latitude and λ the longitude. The data analyzed spans from January 1, 1994 to December 31,
 268 2004. From this data set we study representative days and we also construct climatologies.
 269 Finally, a Runge-Kutta integrator of fourth order and a time step of 6 hours has been
 270 used to obtain backward and forward trajectories in the velocity field for the calculation of
 271 FSLEs and for the advection of a synthetic tracer. The geostrophic velocity field has been
 272 resampled in space and time with a multilinear interpolator.

273 3.2 Sea-surface temperature

274 We used sea-surface temperature (SST) data from the AVHRR sensors on board NOAA
 275 satellites, downloaded from the HRPT station at the Institut de Ciències del Mar (CSIC)
 276 in Barcelona. For the single day analysis we have chosen images for which there were good
 277 quality sea-surface temperature images presenting a large variety of eddy structures and
 278 different intensities of the Algerian current: July 9, 2003; April 7, 2004; June 30, 2004. SST
 279 images have a resolution of 1.1 km at the nadir.

280 4 Results

281 4.1 Eddy representation

282 Figure 2 shows the spatial distribution of OW, which appears as a set of vorticity-dominated
 283 ($W < 0$, blue) regions surrounded by strain-dominated lobular structures ($W > 0$, red)
 284 embedded in a background field of small values of W . On the other hand, Fig. 3 shows the
 285 spatial distribution of FSLEs which has very different patterns characterized by a tangle
 286 of lines. These are the locations where FSLE are large, approximating unstable manifolds
 287 and corresponding to transport barriers embedded in a background field with $\lambda \simeq 0$. The
 288 unstable manifolds arise from fluid stretching and they are therefore Lagrangian analogs of
 289 the deformation OW regions.

290 A first important difference in daily maps of OW and FSLE values is the presence of eddies
 291 in the first and of filaments in the second. In particular, in the FSLE map there are no
 292 enclosed regions and in some cases (e.g. for the eddies over the Balearic abyssal plain), the

293 same manifold connects multiple lobes, spanning a region of several eddies. When comparing
294 these patterns with the stream-function of the flow, SSH in this case, it can be observed
295 that in general eddies localized by the OW parameter and the centers of the spiralling FSLE
296 lobes are in good agreement with the extrema of the altimetric field, as one would expect.
297 Across the Algerian current, the OW field identifies some possibly spurious eddies that do
298 not appear in either the FSLE or SSH. This is due to the fact that both SSH and FSLE
299 are not invariant under a transformation of coordinates to a frame of reference moving at
300 a constant velocity with respect to the original (Galilean transformation) and therefore,
301 eddies are hidden or partially hidden by the presence of the Algerian current. Since OW is
302 Galilean invariant it is able to detect these eddies but it fails in the detection of the Algerian
303 current which appears as a coherent structure characterized by manifolds (barriers) parallel
304 to the altimetric streamlines in the FSLE picture.

305 Another key difference between both fields is linked to the time-evolution of coherent struc-
306 tures. From Figs. 2 and 3 it can be seen that eddies displaying a similar size and intensity
307 in the OW map may show very different features in the FSLE map. This is the case for
308 instance for the western Alboran eddy and some of the mesoscale eddies in the Algerian
309 basin (especially during July 30, 2004). For the Alboran vortex, the lobe spiral is very
310 tight, almost resembling the concentric altimetry lines. For the eddies in the Algerian basin,
311 the lobes are loose, much less localized, and discordant with the altimetric contours. It is
312 interesting to notice that previous studies (e.g. Isern-Fontanet et al., 2006, and references
313 therein) have shown that vortices in the Algerian basin propagate at velocities of the order
314 of 5 km day^{-1} in contrast to the western Alboran eddy, which is almost stationary. In
315 the ideal case of a time-independent velocity field, particle trajectories, as well as the set
316 of lines in which Lyapunov exponents are organized (which approximate material lines),
317 coincide with altimetric isolines. For the case of an eddy, they appear as concentric, closed
318 manifolds. In a time-dependent flow, the identity between trajectories and altimetric iso-
319 lines is lost and the differences quantify the time variability. The material lines resemble
320 concentric circles for slowly evolving persistent structures like the Alboran gyres and as-
321 sume a complex shape in the case of more dynamically active eddies, like the eddies along
322 the Algerian current and some of the eddies over the Algerian basin. This phenomenon
323 has an important effect on the transport properties. Due to the fact that material lines act
324 as transport barriers, eddies with a low time variability and concentric unstable manifolds
325 have a smaller water mass exchange with the surrounding compared to dynamical active
326 vortices (see Lehahn et al. (2007) for a discussion of the eddy time variability in connection
327 with phytoplankton pattern formation).

328 A third important difference between the OW and FSLE approaches is the spatial scale of
329 the structures detected. The OW parameter is bounded by the resolution of the altimetric
330 data ($1/8^\circ$) and the low-pass filters applied during the construction of altimetric maps.
331 This limitation does not hold for the FSLE that is based on trajectory calculations, whose
332 length scale is a combination of both space and time variability of the velocity field. Lobes
333 and filaments below the altimetric resolution appear, especially in the more dynamically
334 active regions, like the fast evolving eddies formed downstream of the Algerian current or
335 the lobes south of the Balearic islands. Very thin filaments are also associated with the
336 Algerian current.

337 4.2 Detection of tracer fronts

338 4.2.1 Synthetic tracer

339 First, we test the ability of OW and FSLE to characterize tracer distribution in an ideal but
340 realistic situation: three sets of particles are advected by the velocity field estimated from
341 altimetry. To this end we put three sets of particles distributed on a square grid centered
342 over three different dynamical structures: the slowly evolving Alboran eddy, the Algerian
343 current, and the strongly interacting eddies in the easternmost part of the Algerian basin
344 (dashed boxes in Fig. 4). Particles in the eddy regions have been advected for two weeks.
345 A shorter advection time of one week has been used for the particles initially placed over
346 the Algerian current, due to the strongest velocity field in this region. The advection time
347 that we have chosen is such that the particles are kept close to the dynamical structures we
348 want to study: a larger advection time does not change the results discussed, but increases
349 the dispersal of the particles over several structures.

350 The tracer released over the west Alboran eddy shows a regular, circular pattern well corre-
351 lated with both the OW and the FSLE maps. This pattern differs from the more deformed
352 distribution for the tracer released over the Algerian basin. In this region, the tracer ap-
353 pears spread on several eddies connected through thin filamentary structures. The bound-
354 aries detected by the OW parameter (we plot in Fig. 4, top, the lines $W = 0$) provide
355 an approximate picture, often underestimating the size of the eddy cores and providing no
356 information of the patterns followed by the tracer exchanged from one eddy to another.
357 In contrast, the FSLE lines of intense stretching reproduce with remarkable accuracy the
358 tracer eddy boundaries, as well as the tangle of spiralling filaments that connect them. This
359 is seen in Fig. 4 (bottom) where we plot the regions where the FSLE has values larger than
360 0.2 day^{-1} . As discussed above, these regions are essentially one-dimensional lines. They
361 behave as material unstable manifolds of the advecting flow: they are almost perfectly lo-
362 cated along the tracer boundary. Small deviations may be attributed to different reasons:
363 (i) a tracer front approaches the manifold exponentially fast, so that a residual distance
364 remains for a finite time of integration; (ii) only the manifolds with an intensity larger than
365 0.2 day^{-1} have been plotted and other weaker lines may also act as transient transport
366 barriers. The residual distance from a manifold can be estimated by Eq. 3: considering an
367 initial tracer to manifold distance of about 100 km , an exponent of $0.2 - 0.3 \text{ day}^{-1}$ for
368 the manifold (Fig. 3), and an advection time of 15 days , we get a separation between the
369 manifold and the tracer front of a few km . Note that the thin filament at 7°W , 37.5°N is
370 below the altimetric resolution, and appears in both the tracer advection and the FSLE
371 map.

372 Thin filaments also appear for the case of the tracer released over the Algerian current.
373 The OW is designed to detect vortices and therefore its use for barrier detection along the
374 Algerian current is, strictly speaking, improper. Nevertheless, the gyre due to the mesoscale
375 eddy located at 0.5°W , 36.5°N is correctly predicted. Not surprisingly, features due to
376 smaller and rapidly evolving eddies (like the ones located along the current), as well as the
377 barrier effect due to the current itself, are not detected. Interestingly, an OW signal appears
378 in correspondence to the Almeria-Oran front (well visible in the southern boundary of the
379 tracer), probably as a signature of the secondary Alboran eddy. Such a signature is composed
380 of broken and irregular structures, but nevertheless is in phase with the southern front of
381 the tracer. The OW does not provide any indication of the filament intruding the Algerian
382 basin. In contrast with the lobular structures detected for eddies, the FSLE shows for the
383 Algerian current meandering lines that follow the African coast. Such lines are in almost
384 perfect agreement with the tracer distribution, well indicating the region of intrusion in

385 the Algerian basin. A spiralling lobe at the location of the eddy also detected by the OW
386 method at 0.5°W , 36.5°N is correctly localized. The Almeria-Oran front is well detected
387 by a manifold that follows uninterrupted the Algerian current, marking a transport barrier
388 that confines the water masses coming from the Alboran sea to an isolated tongue along the
389 African coast. In agreement with this picture, the tracer has no intrusion with such coastal
390 water, being initialized northern to such a manifold.

391 *4.2.2 An observed tracer: SST*

392 Figure 5 depicts the temperature distribution for the three days selected and Fig. 6 shows
393 some zooms corresponding to the dashed squares in Figs. 2, 3 and 5.

394 Figure 6a shows the situation of a relatively isolated westward propagating Algerian vortex.
395 The center of the eddy is well located by the OW parameter, but the strongest SST gradients
396 are beyond the outside of the $W = 0$ which identify the vortex core. FSLE lines reproduce
397 the two-lobe structure of the SST positive anomaly centered in 1E , 37.5N , although the
398 size is overestimated. Furthermore, south of this vortex there is a filament of colder waters
399 that approximately follows the transport barriers depicted by FSLE. However, this example
400 also shows one of the limitations of the approach: FSLE and OW strongly depend on the
401 quality of altimetric maps. A coastal eddy in the Algerian coast is clearly observable in the
402 SST images but is not properly captured by SSH, and therefore partially missed by OW
403 and FSLE.

404 Figure 6b depicts the Alboran sea in spring (April 7, 2004). In its westernmost part, close to
405 the Gibraltar strait, a water mass of warm waters, surrounded by colder waters, is trapped
406 within the western Alboran gyre. Both the OW and the FSLE maps show a regular and
407 circular barrier although both seem to underestimate the radius of the object, maybe due
408 to the location of the vortex in altimetric data. The Almeria-Oran front on the eastern part
409 of the image is observable in both SST and FSLE but not in the OW field. Proceeding to
410 west a large eddy attached to the coast is quite properly identified in all fields: SST, FSLE,
411 SSH and OW. However, in the middle of the image, where the eastern Alboran eddy is
412 usually located there is a poor coincidence between patterns calculated from altimetry and
413 the SST image. In particular, the SST fronts observed at 3°W are almost perpendicular to
414 the FSLE lines there.

415 Figure 6c shows an example of the strong signature of the Algerian current. In contrast with
416 the previous case, the FSLE map reproduces with great accuracy the SST distribution. The
417 dynamical barriers due to the presence of the jet along the coast are parallel to the SST
418 isolines. In analogy to what was observed for the synthetic tracer, the jet has no signature
419 on the OW parameter. On the other hand, several mesoscale eddy boundaries with no effect
420 on the SST pattern also appear in the OW image. Centered at 37°N 2°E there is a large
421 coastal eddy probably generated by the destabilization of the Algerian current. This eddy
422 is clearly identified in all fields. However, the most remarkable pattern is the deflection
423 of coastal waters from coast to the open sea due to the presence of this eddy, which is
424 observable in FSLE as well as in SST. Note also that water masses in the inner part of the
425 vortex are bounded by transport barriers and therefore trapped within the eddy.

426 Finally, Fig. 6d shows the easternmost part of the Algerian basin where several eddies
427 strongly interact. Notice that this is one of the situations analyzed using the advection of
428 ideal particles in the previous section. As expected, the match between real SST data and
429 the FSLE is as good as before. The manifold tangle observed in the FSLE map can also
430 be seen in the SST image and the cores of the eddies on which these manifolds wind are

431 identified also by the OW parameter. An isolated region along the Algerian coast (7E, 37N),
432 appearing in the SST image as a strong cold anomaly, is also fairly well identified by FSLE
433 and not by the OW parameter.

434 4.3 Time averaged fields

435 In order to generalize the comparison performed on instantaneous cases, we focus now on
436 the relationships between spatial field distributions averaged over time. To this end OW
437 and FSLE have been computed for 10 years of data (1994-2004). The OW parameter is
438 calculated for each altimetric image (at one week time resolution) while an FSLE map is
439 generated each two days.

440 4.3.1 Distribution of barrier-type lines

441 First, we estimate the fraction of time during which each spatial point is visited by barrier-
442 type lines. By barrier-type lines we mean lines (ridges made of local maxima in FSLE and
443 the $W = 0$ isolines in OW) which could be interpreted, at least during some short time,
444 as a transport barrier. To this end we count how many times each grid point pertains to
445 one of such lines and divide by the total number of observations for that point (the length
446 of the time-series). Figure 7 shows these local probabilities of having a transport barrier
447 estimated using OW and FSLE (and denoted by P_W and P_λ , respectively). In agreement to
448 what we found in the previous sections, we observe that the pattern corresponding to OW
449 parameter has a more regular, patchy structure due to the presence of Eulerian eddies, and
450 no clear signature for features that are not dependent on individual vortices, like the Algerian
451 current which appears instead in the FSLE map. This suggests the idea that features that
452 are common in both maps might be associated to long-lived non-propagating vortices. The
453 most evident example is the western Alboran eddy. Other examples are the pattern observed
454 around longitude 4°E and 38°N which is associated to the region of vortex detachment from
455 coast discussed in previous papers (Isern-Fontanet et al., 2006), the pattern observed east
456 of Eivissa island (1.5°E and 38.5°N) or the Almeria-Oran front.

457 After observing that OW and FSLE provides very different estimations of the propensity of
458 the points to belong to a barrier-like line, the next question is to identify which one is closer
459 to give a true barrier intensity and location. As outlined in the introduction, a characteristic
460 of the incoming Atlantic waters with respect to the resident Mediterranean ones is their
461 lower salinity. If there are significant barriers to the spread of this surface water into the
462 Mediterranean, climatological distributions of salinity should locate them. Figure 8 shows
463 the climatological salinity obtained from MEDATLAS-II data set. When comparing Figs.
464 7 and 8 it is evident that the estimation computed from FSLE provides a better picture,
465 although the smoothness of the climatological salinity makes difficult the comparison. On
466 Alboran, salinity increases eastwards. Close to the Almeria-Oran front the isohalines are
467 almost aligned width the front, as depicted by FSLE. Eastwards, the intrusion of fresh
468 waters along the coast following the Algerian current and the associated intense northwards
469 gradient matches quite well the patterns observed in Fig. 7 (bottom). Proceeding to the
470 east, at the entrance of the Sardinia channel FSLE barrier density is concentrated close to
471 the coast, in correspondence with low salinity waters being also confined to this area. In
472 the middle of the basin, the probability of having transport barriers is more homogeneous
473 due to the propagation of Algerian eddies and consequently climatological salinity is more
474 uniform.

475 4.3.2 Time averages of FSLE and other Eulerian diagnostics

476 Results in previous sections suggest that high FSLEs are preferentially located on ener-
477 getic structures like at the eddy periphery or along jets. This suggest a possible correlation
478 between the FSLEs and other Eulerian diagnostics different from OW, such as the eddy
479 kinetic energy (EKE) or the strain. In fact, in a recent study of the Tasman sea, it has
480 been shown that averages of both the EKE and the strain have a compact relationship
481 with averages of finite-time Lyapunov exponents (Waugh et al., 2006). Although such rela-
482 tionships are valid only on time average, and therefore cannot be used for the detection of
483 instantaneous, local transport barriers, the correlation between EKE, strain, and Lyapunov
484 exponents would provide a simple way to estimate Lyapunov exponent climatologies, as also
485 suggested in Waugh et al. (2006). Finite-time and finite-size Lyapunov exponents only differ
486 on the determination of the integration time (set a priori for finite-time, given indirectly by
487 prescribing the final separation of the trajectories for finite-size). For this reason, we tested
488 the hypothesis above by computing for our data period time averages of strain rate and of
489 EKE.

490 Climatologies of FSLE, EKE, and strain rate are shown in Fig. 9. Similar structures appear
491 in regions containing persistent objects, such as the Alboran gyre and the Algerian current.
492 A large-scale gradient is also observed, with more signal in the south than in the north of
493 the Algerian basin, and positive anomalies in the Sardinia channel. However, there are more
494 localized mesoscale anomalies in the FSLE field.

495 In Fig. 10, joint distributions of FSLEs vs strain rate and EKE are presented. Although
496 there is a general positive correlation among these quantities, they show a much looser
497 relationship than the one observed by (Waugh et al., 2006) at lower resolution and on shorter
498 integration times. The lack of compact relationships on the scatter plots, as well as different
499 distribution of anomalies among the various diagnostics is a clear confirmation that the
500 Lyapunov exponent provide a complementary information in respect to Eulerian diagnostics
501 even in a climatological sense, when the Lyapunov calculation is done at high resolution. The
502 comparison with other Eulerian diagnostics (like the vorticity and the vorticity gradient,
503 that is sometimes also used for transport barrier detection, see for instance (Paparella et al.,
504 1997)) confirm these observations.

505 5 Summary and discussion

506 In this work we have exploited the rich mesoscale activity of the Algerian basin for comparing
507 Eulerian and Lagrangian diagnostics of transport under various conditions. This comparison
508 unveiled two coexisting pictures: an Eulerian view, dominated by mesoscale eddies, and
509 a Lagrangian view, characterized by interconnected lobular structures and submesoscale
510 filaments. The first picture describes the eddies that populate the mesoscale turbulence;
511 the second one describes the spatial structures of tracers advected by these eddies. Eddy
512 cores are usually identified by setting a threshold ($W = 0$) on the OW parameter, and this
513 $W = 0$ line may be a rough candidate to a ‘transport barrier’ since eddy contents are seen
514 to remain coherent in several situations. More precise candidates to transport barriers are
515 obtained from local maxima (ridges) of the FSLE computed backward in time.

516 As diagnostics of transport barriers, both techniques are based on heuristic arguments
517 related to the time variability of the velocity field. The OW use is based on the consideration
518 that for time-invariant fields, Lagrangian and Eulerian barriers coincide. For this reason,
519 with the OW method no structure typical of time varying fields like filaments and lobular

520 patterns can be detected but nevertheless remarkably good results can be obtained for
521 stationary eddies, in our case the first Alboran gyre and some of the most persistent eddies
522 over the Balearic abyssal plain. The FSLE calculation goes one step further, assuming quasi
523 stationarity not for the velocity field, but for the lines of maximal divergence (unstable
524 manifolds of hyperbolic points). When this time-scale separation between the Lagrangian
525 structures and the advected tracer holds, the tracer front relax exponentially fast over
526 the ridges of large Lyapunov exponents that therefore mark the front position. Another
527 advantage of the FSLE method is that the effect of both eddies and jets are remarkably
528 dealt with.

529 We have tested the barrier candidates against a synthetic tracer advected by the geostrophic
530 field. This test sets an upper limit on the confidence on FSLE and OW assumptions, since it
531 excludes the effect of any factor acting on the tracer except the geostrophic velocity field. At
532 the meso- or larger scales, the OW was found to locate correctly (with errors of tens of km)
533 tracer patches when they were well confined inside eddies. Fluid parcels intruding eddies's
534 along thin filaments are not captured however. Such filaments, as well as the submesoscale
535 structure of tracer fronts, were found from the FSLE calculations.

536 In fact, the advection of a synthetic tracer can be considered itself as a direct, Lagrangian
537 diagnostic of transport barriers. This approach however has some limitations. Lagrangian
538 structures are sampled unevenly, since the tracer tends to spend longer times in regions with
539 low velocities. For this reason, even strong barriers may require a carefully choice of the
540 initial conditions and of the integration time. An example of this appears in Fig. 4, where
541 part of the Almerian-Oran front is not entirely visible and would have required to probe
542 the velocity field with a larger number of tracer blobs. When doing the tracer experiment of
543 Fig. 4 we also observed that, not surprisingly, the tracer has a long residence time over the
544 Balearic Abyssal Plain and therefore for long integration times most of the time the tracer
545 shades the barrier of this region only, independently of its initial condition. On the other
546 hand, a reduction of the integration time increases the gap between the tracer front and
547 the actual barrier position, since the tracer front has a shorter time to relax to it (see the
548 discussion of Eq. 3). In fact, an attempt to overcome these limitations requires the use of
549 backward trajectories (for which barriers are regions of maximal separation) and of variable
550 integration times, basically yielding a FSLE-type calculation. For this reason, the FSLE can
551 be considered an optimised way of advecting a passive tracer for the detection of transport
552 structures. Note also that, besides guaranteeing a uniform sampling of the velocity field and
553 the precise localization of transport barriers, the FSLE also provides the information of the
554 intensity of the barrier at the same cost of tracer advection.

555 The representation of advection in the Algerian basin however is based on altimetry and
556 therefore is limited by the lack of representation of any non-geostrophic component of the
557 velocity field as well as unresolved or poorly resolved structures due to space and time
558 resolution (Pascual et al., 2006), and noise. The comparison with SST images allows to
559 verify that such effects are not strong enough to spoil the FSLE usefulness in locating
560 Lagrangian features. Note that the filament tangle connecting different eddies as well as the
561 spiral structures inside eddy cores cannot appear in any way in a time-independent field
562 (i.e., by using a snapshot of the velocity field), where one can show that orbits correspond
563 to altimetric contours, and eddy barriers to closed contours. Nevertheless, the slow time
564 variability of a few altimetric frames is enough to generate Lagrangian structures which
565 correspond well to SST images. We also expected an effect of altimetric errors especially
566 for the structures close to the coast, but with the exception of the position of the first
567 gyre in the Alboran sea and in spite of the chaotic nature of the geostrophic advection, the
568 localization of features from Lyapunov exponent maps appears quite reliable.

569 Climatologies of several Eulerian diagnostics and either barrier densities or average values

570 of Lyapunov exponents also showed distinct different patterns. Given the fact that the main
 571 differences between Lyapunov and Eulerian diagnostics are related to small scale filaments
 572 and in the temporal variability of mesoscale turbulence, it is not difficult to expect different
 573 relation between Eulerian diagnostics and Lyapunov exponents computed at much larger
 574 scale and on shorter time periods. This is the case of the 0.5 deg. and 15 days calculation
 575 of in Waugh et al. (2006) (resp. 50 times larger and 3 times shorter than in our case).
 576 We illustrate this in Fig. 11, where the Lyapunov exponents have been computed with
 577 initial separations of 0.5 deg. for the same day of Fig. 3a. Indeed, at the resolution of
 578 the Mediterranean altimetry product (1/8 deg.) not even the patterns of two Eulerian
 579 diagnostics like the strain and the eddy kinetic energy appear to be correlated (Fig. 9 b
 580 and c). An interesting exercise would be the calculation of correlation between eddy kinetic
 581 energy and Lyapunov exponents computed at various scales, in order to see whether there
 582 exists a critical lengthscale or a smooth transition. In fact, the finite-size Lyapunov exponent
 583 has been introduced in turbulence theory with the aim of probing a velocity field at various
 584 scales. General arguments (Aurell et al., 1997) suggest the presence of a cross-over scale
 585 in the Lyapunov calculation separating an exponential regime from other diffusive regimes
 586 at the scale of the smallest resolved eddy. For the case of altimetry, this cross-over can be
 587 expected to appear at spatial scales of the order of 1 deg.

588 Note that the Lyapunov exponent is not an advanced replacement of Eulerian diagnostics,
 589 but a complementary tool incorporating tracer information. For instance, the association of
 590 lobes with eddies that in some cases we observed only holds for stationary eddies. If used
 591 systematically as a Lagrangian eddy detection, this approach would lead to detect spurious,
 592 small-scale spatial signal, that in fact comes from the temporal variability of large-scale
 593 eddies. The OW and FSLE method are also complementary from a technical viewpoint. The
 594 OW method is a differential technique. It is thus affected by small-scale noise and especially
 595 by discontinuities. These kind of features indeed can appear in the presence of eddies with a
 596 size close to the spatial resolution. On the contrary, the FSLEs are computed by integrating
 597 particle trajectories and thus are not strongly affected by local noise or discontinuities. The
 598 complementarity of the information detected by FSLE in respect to the OW parameter and
 599 other Eulerian diagnostics is also emphasised in the climatologies of Fig. 7 that showed how
 600 the differences detected in single day analyses are indeed a persistent feature.

601 The main drawbacks of the FSLEs are a relatively increased complexity in the calculation
 602 (with respect to the OW) and especially the need of extended velocity data sets, both in
 603 time and in space. This can be a problem if the observational region is limited (either in
 604 time or space), since some trajectories may go out from the boundaries (this is in fact at
 605 the basis of other methods used to characterize flow structures (Schneider et al., 2005)).

606 The OW on the contrary can be calculated from a snapshot of the velocity field. Indeed,
 607 its easiness allows to compute it even from in situ data (e.g. Stocker and Imberger, 2003;
 608 Testor and Gascard, 2005; Pallás and Víudez, 2005) and then obtain a first approach to
 609 the flow topology and its effect on the transport. Furthermore, although OW is a dif-
 610 ferential technique and therefore more sensible to velocity errors or discontinuities, it is
 611 possible to approach it using kinetic energy at least for the identification of vortex core
 612 edges (Paparella et al., 1997; Isern-Fontanet et al., 2004). If the vortex is assumed to be
 613 close to axial symmetry then the OW formula can be written as

$$614 \quad W \propto \frac{1}{r} \left(\frac{\partial E(r)}{\partial r} \right), \tag{6}$$

615 where r is the radius from the vortex center and $E(r)$ its density of kinetic energy at that
 616 distance from the center. This implies that the line of $W = 0$ will correspond to a local

617 maximum of energy.

618 The comparison with SST and synthetic tracer patterns also shows that the errors in the
619 OW method and the FSLE technique are of very different nature. The OW fails with both
620 the real and synthetic tracer mainly for detection of the filamentation process, due to its
621 intrinsic lack of representation of the time variability of the velocity field. In contrast, the
622 FSLE is limited not by its assumption of time-scale separation between barrier and tracer,
623 but because of the limits of the altimetric data. This is clearly shown by the fact that the
624 FSLE performs almost ideally for the synthetic case while only providing a more qualitative
625 estimations of SST fronts. In perspective, envisaging the availability of assimilation and
626 observational velocities field of increased quality and spatiotemporal resolution, one can
627 expect a decrease in effectiveness of the OW technique in favour of the FSLE (or any other
628 Lagrangian technique) at least for the detection of (sub-)mesoscale transport barriers.

629 6 Conclusions

630 The advantages of a Lagrangian tool when compared to Eulerian diagnostics in capturing
631 tracer structures would be trivial for model data. What is not trivial is that altimetry
632 data are amenable to such a comparison, given that the differences arise in presence of
633 tracer filaments, i.e., at a scale similar or even smaller than the nominal resolution of
634 altimetry data (and much smaller than the cutoff in the altimetry energy spectrum). At
635 this scale ageostrophic components (unresolved by altimetry data) as well as SST active
636 dynamics is supposed to play an important role. The fact that nevertheless altimetry-derived
637 patterns approach SST structures means that these unresolved components of the flow
638 are either of weak intensity or act in phase with the horizontal stirring (Lehahn et al.,
639 2007). The recent availability of realistic, submesoscale resolving biogeochemical models
640 (e.g. (Resplandy et al., 2008)) should give the possibility of exploring the role of unresolved
641 ageostrophic components and of tracer activity on filament detection.

642 The fact that altimetry data can be pushed at subgrid scales when re-analysed by Lagrangian
643 tools, providing systematic information of filament location, opens several interesting per-
644 spectives. For the case of high-resolution biogeochemical measurements, the Lyapunov ex-
645 ponent provides an unpaired tool helping to interpret the measurements in terms of the
646 precise position of mesoscale and sub-mesoscale fronts. The use of Lyapunov calculation
647 can be even concieved in real-time, for targetting frontal structures during in-situ surveys.
648 This possibility comes from the fact that the Lyapunov calculation only requires the past
649 history of the velocity field, and from the availability of altimetry products with 1-2 weeks
650 of delays (e.g. from AVISO).

651 A second interesting possibility is the use of the Lyapunov exponent together with high-
652 resolution tracer measurments for the validation of a velocity field. An improved altimetry
653 product (as what is expected from the recent launch of Jason-2 and incoming altimetry
654 satellites) should bring a velocity field at better spatial and temporal resolution. The pos-
655 sibility of computing with Lyapunov calculation the position of fronts and of comparing
656 them with high-resolution SST or chlorophyll images is one of the very few possibilities for
657 testing the ability of the new products of better representing mesoscale and sub-mesoscale
658 processes. This validation would be especially useful for choosing the optimal combination
659 of spatial and temporal resolution of surface current products. A similar approach can be
660 used also for validating assimilation products and in general for tuning the spatiotemporal
661 resolution of circulation models.

662 Given the fact that transport barriers in the ocean evolves on a much slower time scale than
663 advected tracers, one can also approximate the short-time advection of a released tracer as
664 a relaxation dynamics towards the stronger transport barriers and in this way estimate the
665 tracer distribution in the near future. The most evident application of this system would
666 be, for example, the prediction of the evolution of pollutants. Other Lagrangian techniques
667 have already approached this problem (Lekien et al., 2005).

668 7 Acknowledgments

669 This work is a contribution to the FISICOS (FIS2007-60327) project of the Spanish MEC
670 and PIF project OCEANTECH of the Spanish CSIC. FdO has been supported by Marie-
671 Curie grant 024717-DEMETERA and CNES. JIF has been supported by Marie-Curie grant
672 041476-OCEAN3D. The altimeter products were produced by Ssalto/Duacs and distributed
673 by Aviso, with support from CNES (<http://www.aviso.oceanobs.com>). AVHRR data were
674 obtained from the SAIDIN database at ICM (<http://ers.cmima.csic.es/saidin/>). We ac-
675 knowledge the help received from Marie-Hélène Rio, Alejandro Morales and Isabelle Taupier-
676 Létage.

677 References

- 678 Abraham, E., 1998. The generation of plankton patchiness by turbulent stirring. *Nature*
679 391 (5), 577–580.
- 680 Abraham, E., Bowen, M., 2002. Chaotic stirring by a mesoscale surface-ocean flow. *Chaos*
681 12, 373–381.
- 682 Abraham, E. R., Law, C. S., Boyd, P. W., Lavender, S. J., Maldonado, M. T., Bowie,
683 A., 2000. Importance of stirring in the development of an iron-fertilized phytoplankton
684 bloom. *Nature* 407, 727–730.
- 685 Artale, V., Boffetta, G., Celani, A., Cencini, M., Vulpiani, A., 1997. Dispersion of passive
686 tracers in closed basins: Beyond the diffusion coefficient. *Phys. Fluids* 9, 3162–3171.
- 687 Aurell, E., Boffetta, G., Crisanti, A., Paladin, G., Vulpiani, A., 1997. Predictability in the
688 large: an extension of the Lyapunov exponent. *J. Phys. A* 30, 1–26.
- 689 Basdevant, C., Philipovitch, T., 1994. On the validity of the "Weiss criterion" in two-
690 dimensional turbulence. *Physica D* 113, 17–30.
- 691 Boffetta, G., Lacorata, G., Redaelli, G., Vulpiani, A., 2001. Detecting barriers to transport:
692 a review of different techniques. *Physica D* 159, 58–70.
- 693 Bouzinac, C., Vázquez, J., Font, J., 1998. CEOF analysis of ERS-1 and
694 TOPEX/POSSEIDON combined altimetric data in the region of Algerian current.
695 *J. Geophys. Res.* 103, 8059–8071.
- 696 Boyd, P., Watson, A. J., Law, C. S., et al., 2000. A mesoscale phytoplankton bloom in the
697 polar southern ocean stimulated by iron fertilization. *Nature* 407, 695–702.
- 698 Bracco, A., LaCasce, J., Pasquero, C., Provenzale, A., 2000. The velocity distribution of
699 barotropic turbulence. *Phys. Fluids* 12 (10), 2478–2488.
- 700 Bradbury, I., Snelgrove, V. R., 2001. Contrasting larval transport in demersal fish and
701 benthic invertebrates: The roles of behaviour and advective processes in determining
702 spatial pattern. *Can. J. Fish. Aquatic Sci.* 58, 811–823.
- 703 Bresseur, P., Beckers, J. M., Brankart, J., Shoenauen, R., 1996. Seasonal temperatures and
704 salinity fields in the Mediterranean sea: climatological analysis of a historical data set.
705 *Deep-Sea Res. I* 43, 159–192.

- 706 Chaigneau, A., Pizarro, O., 2005. Eddy characteristics in the eastern south pacific. *J. Geo-*
707 *phys. Res.* 110, C06005.
- 708 Coulliette, C., Wiggins, S., 2001. Intergyre transport in a wind-driven, quasigeostrophic
709 double gyre: An application of lobe dynamics. *Nonlin. Proc. in Geophys.* 8, 69–94.
- 710 d’Ovidio, F., Fernández, V., Hernández-García, E., López, C., 2004. Mixing structures in the
711 mediterranean sea from finite-size lyapunov exponents. *Geophys. Res. Lett.* 31, L17203.
- 712 Elhmaïdi, D., Provenzale, A., Babiano, A., 1993. Elementary topology of two-dimensional
713 turbulence from a Lagrangian viewpoint and single-particle dispersion. *J. Fluid Mech.*
714 257, 533–558.
- 715 Font, J., Isern-Fontanet, J., Salas, J., 2004. Tracking a big anticyclonic eddy in the Algerian
716 basin (Western Mediterranean Sea). *Sci. Mar.* 68 (3), 331–342.
- 717 García-Olivares, A., Isern-Fontanet, J., García-Ladona, E., 2005. Dispersion of passive trac-
718 ers and Finite-Scale Lyapunov Exponents in the Western Mediterranean sea. *Deep-Sea*
719 *Res. II* 54, 253–268.
- 720 Haller, G., 2001. Distinguished material surfaces and coherent structures in three-
721 dimensional fluid flows. *Physica D* 149, 248–277.
- 722 Haller, G., Yuan, G., 2000. Lagrangian coherent structures and mixing in two-dimensional
723 turbulence. *Physica D* 147, 352–370.
- 724 Hua, B., Klein, P., 1998. An exact criterion for the stirring properties of nearly two-
725 dimensional turbulence. *Physica D* 113, 98–110.
- 726 Hua, B., McWilliams, J., Klein, P., 1998. Lagrangian accelerations in geostrophic turbulence.
727 *J. Fluid Mech.* 366, 87–108.
- 728 Isern-Fontanet, J., Font, J., Garcia-Ladona, E., Emelianov, M., Millot, C. and Taupier-
729 Letage, I., 2004. Spatial structure of anticyclonic eddies in the Algerian basin (Mediterranean Sea) analyzed using the Okubo-Weiss parameter. *Deep-Sea Res. II* 51, 3009–3028.
- 730 Isern-Fontanet, J., García-Ladona, Font, J., 2003. Identification of marine eddies from al-
731 timetry. *J. Atmos. Oceanic Technol.* 20, 772–778.
- 732 Isern-Fontanet, J., García-Ladona, Font, J., 2006. The vortices of the Mediterranean sea:
733 an altimetric viewpoint. *J. Phys. Oceanogr.* 36 (1), 87–103.
- 734 Iudicone, D., Lacorata, G., Rupolo, V., Santoleri, R., Vulpiani, A., 2002. Sensitivity of
735 numerical tracer trajectories to uncertainties in OGCM velocity fields. *Ocean Modelling*
736 4 (3-4), 313–325.
- 737 Jeong, J., Hussain, F., 1995. On the identification of a vortex. *J. Fluid Mech.* 285, 69–94.
- 738 Joseph, B., Legras, B., 2002. Relation between kinematic boundaries, stirring and barriers
739 for the Antarctic Polar Vortex. *J. Atmos. Sci.* 59, 1198–1212.
- 740 Koh, T., Legras, B., 2002. Hyperbolic lines and the stratospheric polar vortex. *Chaos* 12 (2),
741 382–394.
- 742 LaCasce, J., Ohlmann, C., 2003. Relative dispersion at the surface of th Gulf of Mexico. *J.*
743 *Mar. Res.* 61 (3), 285–312.
- 744 Lacorata, G., Aurell, E., Vulpiani, A., 2001. Drifter dispersion in the adriatic sea: Lagrangian
745 data and chaotic model. *Ann. Geophysicae* 19, 121–129.
- 746 Lapeyre, G., Klein, P., Hua, B., 1999. Does the tracer gradient vector align with strain
747 eigenvectors in 2d turbulence? *Phys. Fluids* 11 (12), 3729–3737.
- 748 Lapeyre, G., Klein, P., Hua, B. L., 2006. Oceanic restratification forced by surface fronto-
749 genesis. *J. Phys. Oceanogr.* In press.
- 750 Larnicol, G., Ayoub, N., Le Traon, P., 2002. Major changes in the Mediterranean sea level
751 variability from 7 years of TOPEX/POSEIDON ERS-1/2 data. *J. Mar. Syst.* 33–34,
752 63–89.
- 753 Le Traon, P., Nadal, F., Ducet, N., 1998. An improved mapping method of multisatellite
754 altimeter data. *J. Atmos. Oceanic Technol.* 15, 522–534.
- 755 Legal, C., Klein, P., Treguier, A.-M., Paillet, J., 2006. Diagnostics of the vertical motions
756 in a mesoscale stirring region. *J. Phys. Oceanogr.* 37, 1413–1424.
- 757 Lehahn, Y., d’Ovidio, F., Lévy, M., Heyfetz, E., 2007. Stirring of the Northeast Atlantic
758 spring bloom: a lagrangian analysis based on multi-satellite data. *J. Geophys. Res.* 112,

760 C08005.

761 Lekien, F., Coulliette, C., Mariano, A. J., Ryan, E. H., Shay, L. K., Haller, G., Marsden, J.,
762 2005. Pollution release tied to invariant manifolds: A case study for the coast of Florida.
763 *Physica D* 210, 1–20.

764 Lévy, M., Klein, P., Treguier, A.-M., 2001. Impact of sub-mesoscale physics on production
765 and subduction of phytoplankton in an oligotrophic regime. *J. Mar. Res.* 59, 535–565.

766 Lévy, M., Lehahn, Y., Andre, J.-M., Mémery, L., Loisel, H., Heifetz, E., 2005. Production
767 regimes in the Northeast Atlantic: A study based on SeaWiFS chlorophyll and OGCM
768 mixed layer depth. *J. Geophys. Res.* 110, 10.1029/2004JC002771.

769 López, C., Neufeld, Z., Hernández-García, E., Haynes, P., 2001. Chaotic advection of re-
770 acting substances: Plankton dynamics on a meandering jet. *Phys. Chem. Earth B* 26,
771 313–317.

772 Mancho, A., Small, D., Wiggins, S., 2006. A tutorial on dynamical systems concepts applied
773 to Lagrangian transport in oceanic flows defined as finite time data sets. *Phys. Rep.* 437,
774 55–124.

775 Martin, A., 2003. Phytoplankton patchiness: the role of lateral stirring and mixing. *Progress*
776 *in Oceanography* 57, 125–174.

777 Martin, A., Richards, K. J., Bracco, A., Provenzale, A., 2002. Patchy productivity in the
778 open ocean. *Global. Biogeochem. Cycles* 16, 10.1029/2001GB001449.

779 McGillicuddy, D. J., Robinson, A. R., Siegal, D. A., Jannasch, H. W., Johnson, R., Dicky,
780 T. D., Mcneil, J., Michaels, A. F., Knap, A. H., 1998. Influence of mesoscale eddies on
781 new production in the Sargasso Sea. *Nature* 394, 263–265.

782 Miller, P., Jones, C., Rogerson, A., Pratt, L., 1997. Quantifying transport in numerically
783 generated velocity fields. *Physica D* 110, 105–122.

784 Millot, C., 1999. Circulation in the western Mediterranean sea. *J. Mar. Syst.* 20, 423–442.

785 Millot, C., Benzohra, M., Taupier-Letage, I., 1997. Circulation off algeria infered from the
786 médiprod-5 current meters. *Deep-Sea Res. I* 44, 1467–1495.

787 Morrow, R., Birol, F., Griffin, D., Sudre, J., 2004. Divergent pathways of cyclonic and
788 anti-cyclonic ocean eddies. *Geophys. Res. Lett.* 31, L24311.

789 Okubo, A., 1970. Horizontal dispersion of floatable particles in the vicinity of velocity
790 singularities such as convergences. *Deep-Sea Res.* 17, 445–454.

791 Ovchinikov, I., 1966. Circulation in the surface and intermediate layers of the Mediterranean.
792 *Oceanology* 6, 48–59.

793 Paci, A., Caniaux, G., Gavart, M., Giordani, H., Lévy, M., Prieur, L., Reverdin, G.,
794 2005. A high resolution simulation of the ocean during the POMME experiment.
795 part 1 : simulation results and comparison with observations. *J. Geophys. Res.* 110,
796 10.1029/2004JC002712.

797 Pallás, E., Víudez, A., 2005. Diagnosing mesoscale vertical motion from horizontal velocity
798 and density data. *J. Phys. Oceanogr.* 35, 1744–1762.

799 Paparella, F., Babiano, A. Basdevant, C., Provenzale, A., Tanga, P., 1997. A Lagrangian
800 study of the Antarctic polar vortex. *J. Geophys. Res.* 102 (D6), 6765–6773.

801 Pascual, A., Faugère, Y., Larnicol, G., Le Traon, P., 2006. Improved description of the
802 ocean mesoscale variability by combining four satellite altimeters. *Geophys. Res. Lett.*
803 33, L02611, doi:10.1029/2005GL024633.

804 Pasquero, C., Provenzale, A., Babiano, A., 2001. Parametrization of dispersion in two-
805 dimensional turbulence. *J. Fluid Mech.* 439, 279–303.

806 Pierrehumbert, R., 1991. Large-scale horizontal mixing in planetary atmospheres. *Phys.*
807 *Fluids A* 3 (5), 1250–1260.

808 Puillat, I., Taupier-Letage, I., Millot, C., 2002. Algerian eddies lifetime can near 3 years. *J.*
809 *Mar. Syst.* 31, 245–259.

810 Resplandy, L., Lévy, M., d’Ovidio, F., Marlivat, L., 2008. Evidence of submesoscale dynam-
811 ics in pCO₂ sequestration. Submitted to *Global Biogeochem. Cycles* .

812 Ridderinkhof, H., Zimmerman, J., 1992. Chaotic stirring in a tidal system. *Science* 258,
813 1107–1111.

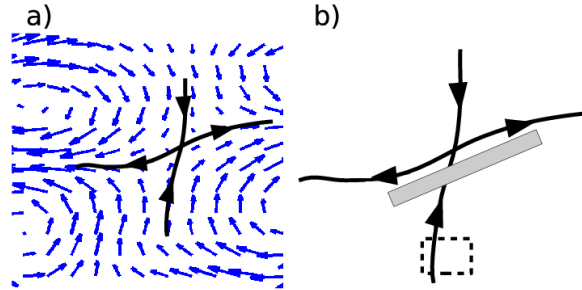


Fig. 1. A sketch of a hyperbolic structure (a) and its effect on an tracer advected by the velocity field and initialised in the dashed region (b). The unstable manifold acts as a transport barrier and generates a front, while the stable manifold cannot be directly compared with the tracer distribution. A more quantitative picture is presented in Fig. 4b.

- 814 Rio, M.-H., Poulain, P.-M., Pascual, A., Mauri, E., Larnicol, G., 2007. A mean dynamic
815 topography of the Mediterranean sea computed from altimetric data and in-situ mea-
816 surements. *J. Mar. Syst.* 65, 484–508.
- 817 Robinson, A. R. et al., 1993. Mesoscale and upper ocean variabilities during the 1989 JGOFS
818 bloom study. *Deep-Sea Res. II* 40, 9–35.
- 819 Rossi, V., López, C., Sudre, J., E., H.-G., Garçon, V., 2008. Comparative study of mixing
820 and biological activity of the Benguela and Canary upwelling systems. *Geophys. Res.*
821 *Lett.* 35, L11602, doi:10.1029/2008GL033610.
- 822 Sallee, J. B., Speer, K., Morrow, R. M., Lumpkin, R., 2007. An estimate of Lagrangian eddy
823 statistics and diffusion in the mixed layer of the southern ocean. Submitted to *Journal*
824 *of Climate* Submitted.
- 825 Sallee, J. B., Wienders, K., Speer, K., Morrow, R. M., 2006. Formation of subantarctic mode
826 water in the southeastern Indian Ocean. *Ocean Dynamics* 56, 525–542.
- 827 Schneider, J., Fernández, V., Hernández-García, E., 2005. Leaking method approach to
828 surface transport in the Mediterranean Sea from a numerical ocean model. *J. Mar. Syst.*
829 57, 111–126.
- 830 Shadden, S. C., Lekien, F., Marsden, J. E., 2005. Definition and properties of Lagrangian
831 structures from finite-time Lyapunov exponents in two-dimensional aperiodic flows. *Phys-*
832 *ica D* 212, 271–304.
- 833 SSALTO/DUACS User Handbook, January 2006. (M)SLA and (M)ADT Near-Real Time
834 and Delayed Time Products. CLS-DOS-NT-06.034.
- 835 Stocker, R., Imberger, J., 2003. Horizontal transport and dispersion in the surface layer of
836 a medium-sized lake. *Limnol. Oceanogr.* 48, 971–982.
- 837 Testor, P., Gascard, J.-C., 2005. Large-scale flow separation and mesoscale eddy formation
838 in Algerian basin. *Progress in Oceanography* 66, 211–230.
- 839 Toner, M., Kirwan Jr, A., Poje, A., Kantha, L., Muller-Karger, F., Jones, C., 2003. Chloro-
840 phyll dispersal by eddy-eddy interactions in the gulf of mexico. *J. Geophys. Res.* 108,
841 10.1029/2002JC001499.
- 842 Vignudelli, S., 1997. Potential use of ERS-1 an Topex/Posseidon altimeters for resolving
843 oceanographic patterns in the Algerian Basin. *Geophys. Res. Lett.* 24 (14), 1787–1790.
- 844 Waugh, D., Abraham, E., Bowen, M., 2006. Spatial variations of stirring in the surface
845 ocean: A case study of the Tasman sea. *J. Phys. Oceanogr.* 36 (3), 526–542.
- 846 Weiss, J., 1991. The dynamics of enstrophy transfer in two-dimensinal hydrodynamics.
847 *Physica D* 48, 273–294.
- 848 Young, W. R., Rhines, P. B., Garrett, C. J. R., 1982. Shear-flow dispersion, internal waves
849 and horizontal mixing in the ocean. *J. Phys. Oceanogr.* 12, 515–527.

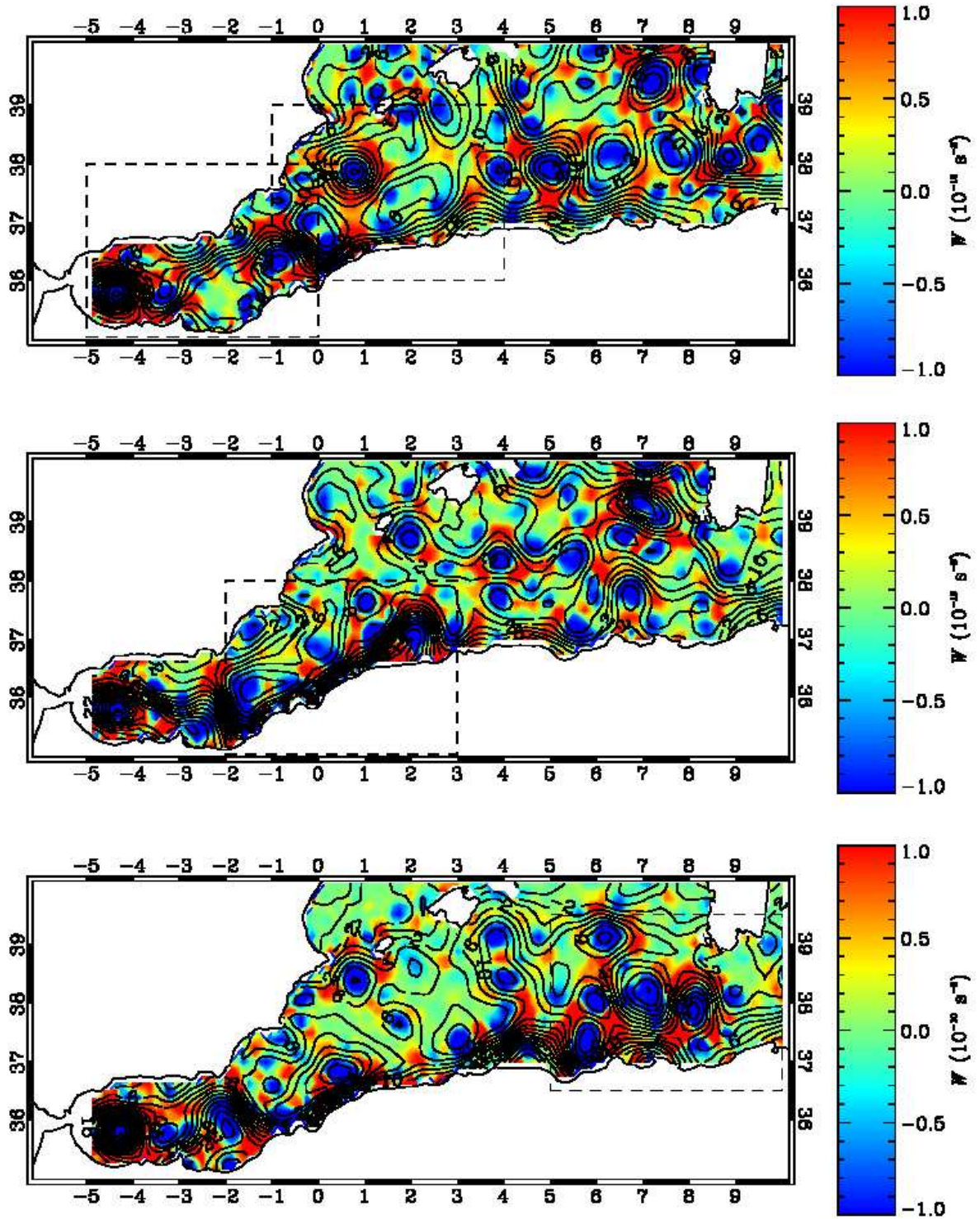


Fig. 2. Okubo-Weiss parameter (W , coded in colors) computed from sea-surface height (black line) fields corresponding (from top to bottom) to July 9, 2003; April 7, 2004; June 30, 2004. The dashed boxes represent the regions over which we perform a comparison with SST (see Figs. 5 and 6).

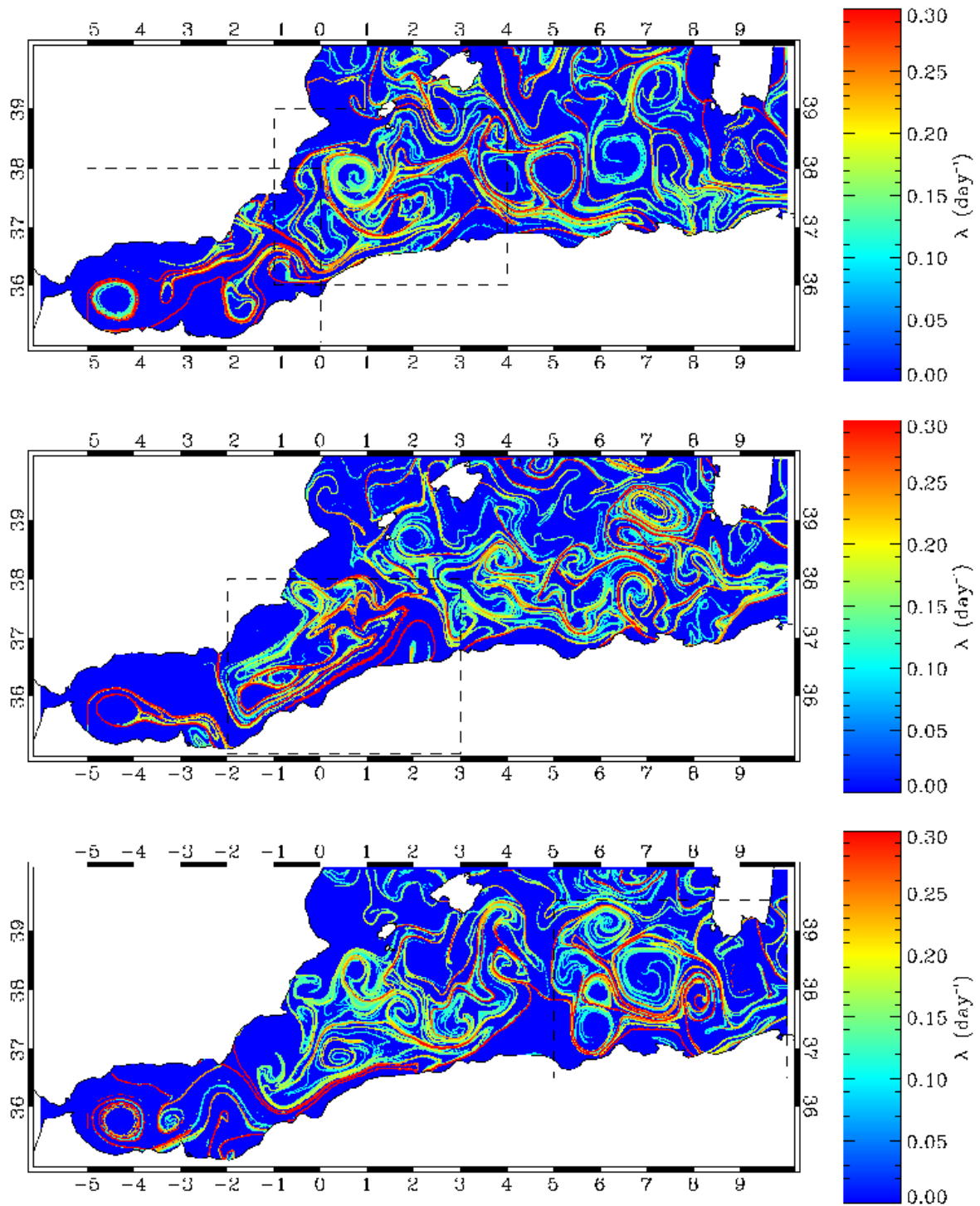


Fig. 3. FSLE (λ) computed from sea-surface height fields corresponding (from top to bottom) to July 9, 2003; April 7, 2004; June 30, 2004. The dashed boxes represent the regions over which we perform a comparison with SST (see Fig. 5).

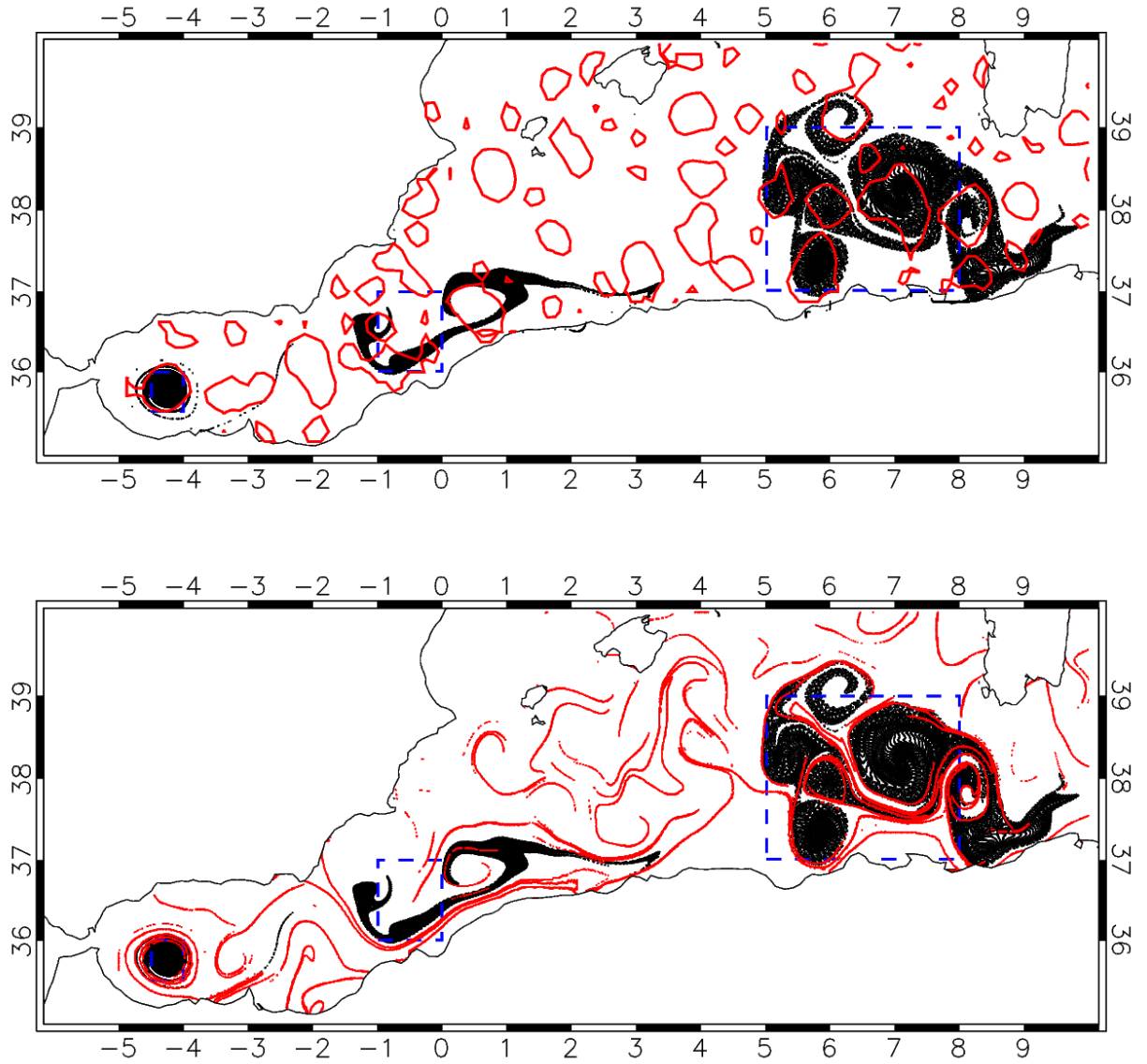


Fig. 4. Distribution of tracer particles released over the Algerian current, the western Alboran eddy, and the easternmost part of the Algerian basin (dotted boxes). Tracers in the Algerian current are advected for one week, and the other two sets are advected for two weeks. The release dates are chosen to have for the three cases the coinciding final time (June 30, 2004) which is shown in the figure. Zero-lines of OW corresponding to the final day are overimposed (top) as well as the line-shaped regions where the backwards FSLE values are larger than 0.2 days^{-1} (bottom), approximating unstable manifolds of the chaotic flow.

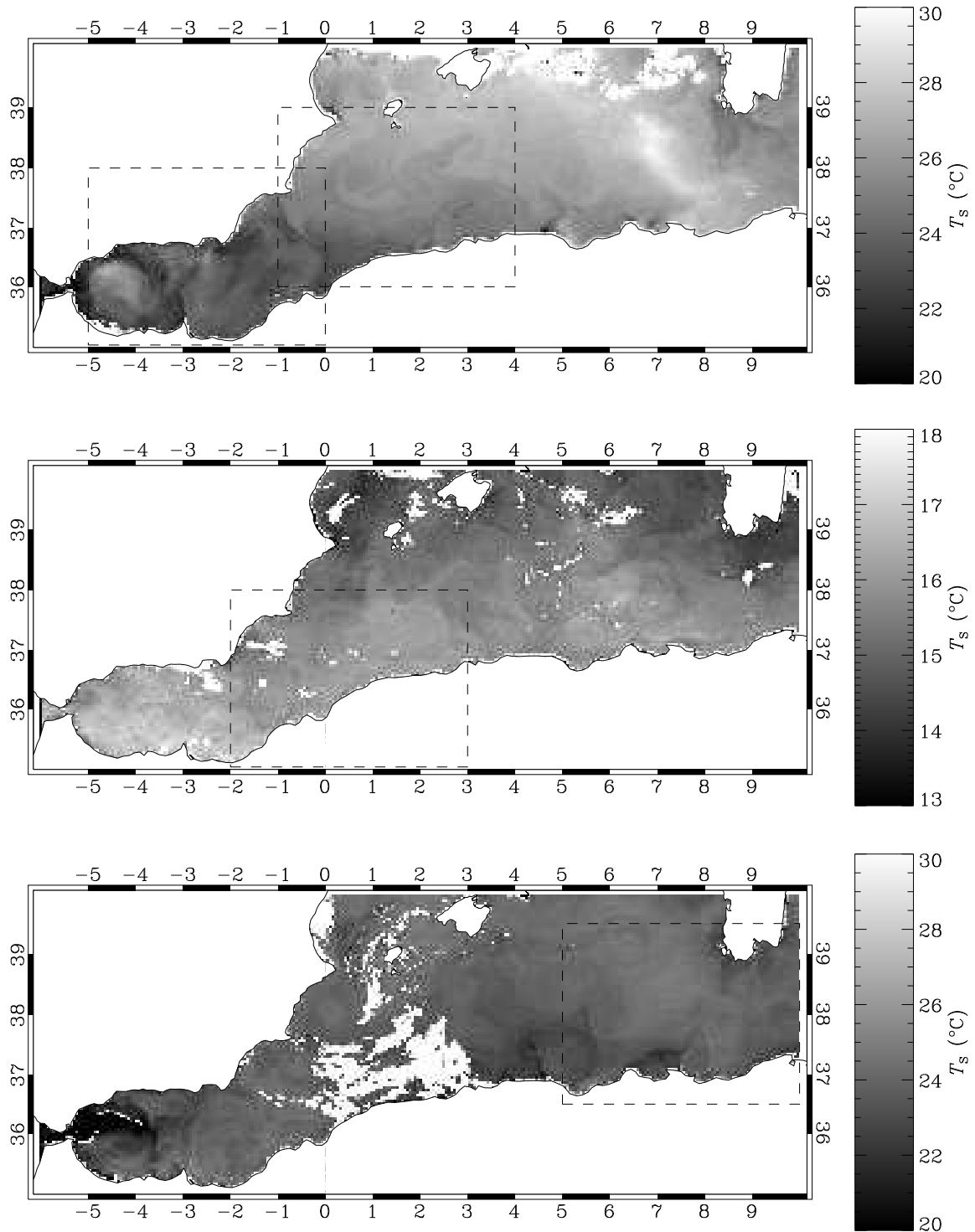


Fig. 5. General views of the sea-surface temperature fields corresponding (from top to bottom) to July 9, 2003; April 7, 2004; June 30, 2004.

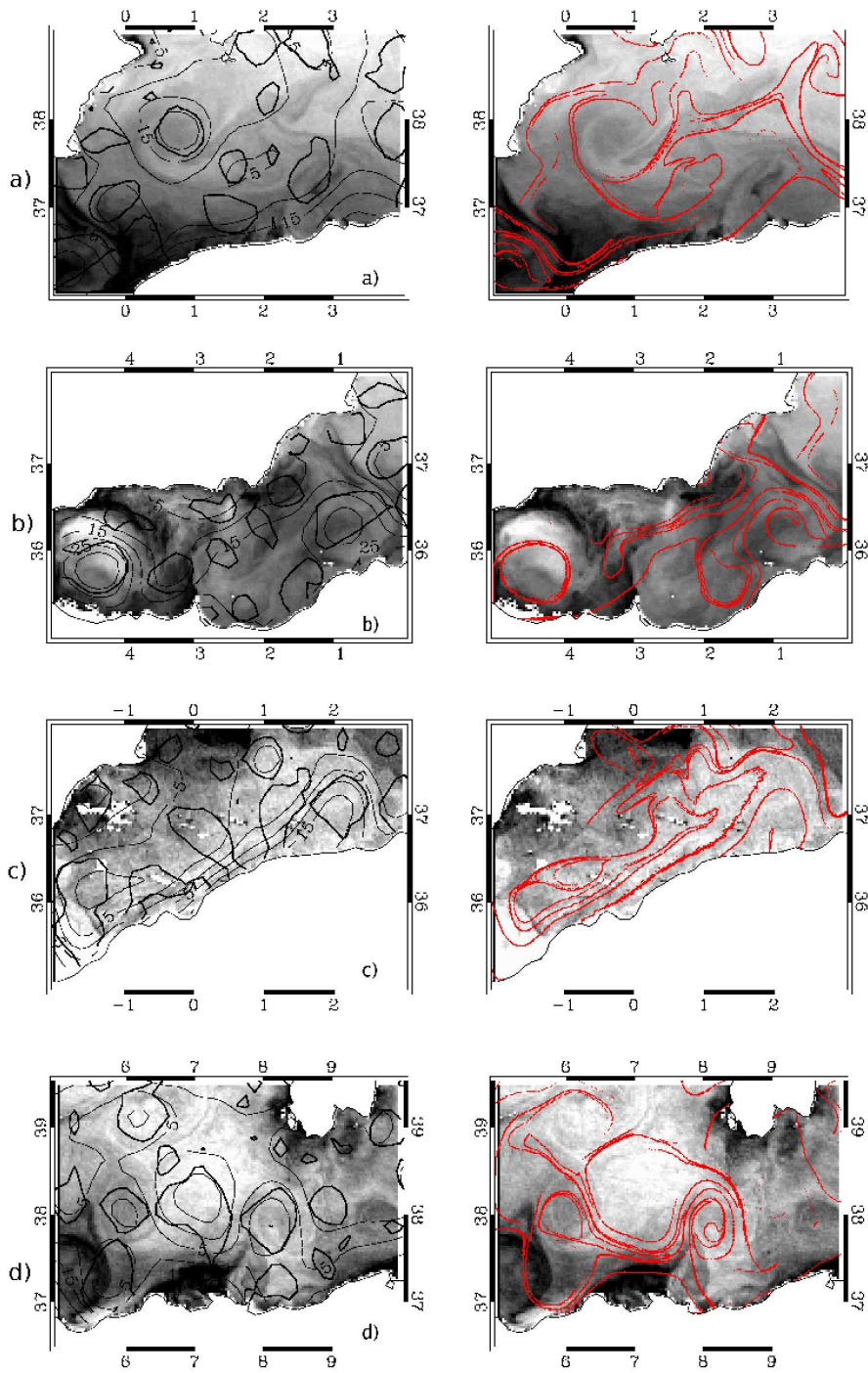


Fig. 6. Comparison of OW, FSLE and temperature distribution corresponding to the regions shown in figures 2-5. Left column: SST (coded in grey levels) with SSH (thin black line) and lines of zero OW (thick black line). Right column: SST (in grey levels) with regions where FSLE is greater than 0.1 day^{-1} (red line-shaped regions). From top to bottom the dates are: July 9, 2003 (a and b); April 7, 2004 (c) and July 2, 2004 (d).

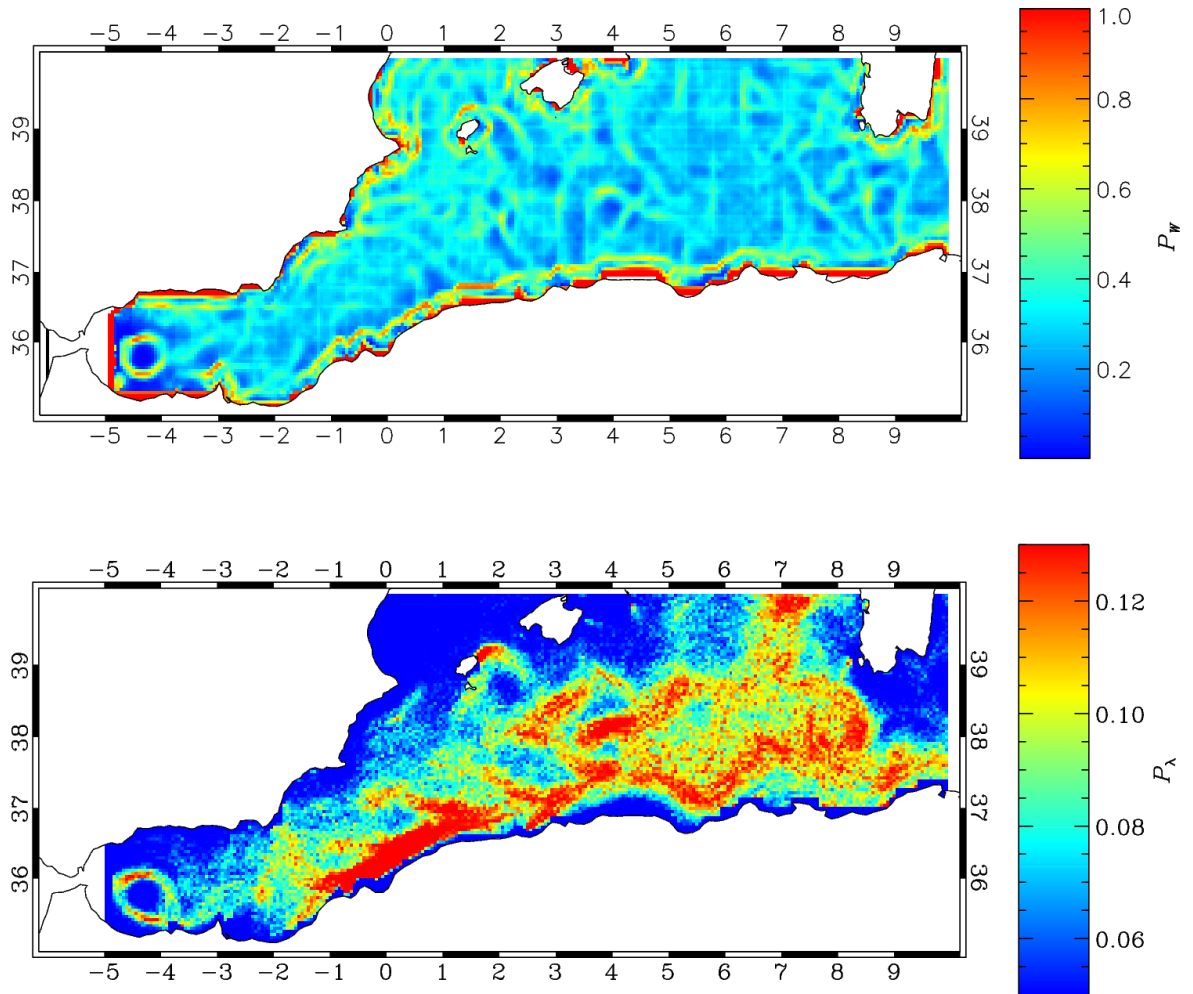


Fig. 7. Fraction of time during which each spatial point is visited by the lines $W = 0$ (P_W , upper panel) and by the ridges (local maxima along some direction) of FSLE (P_λ , lower panel) for the period 1994-2004.

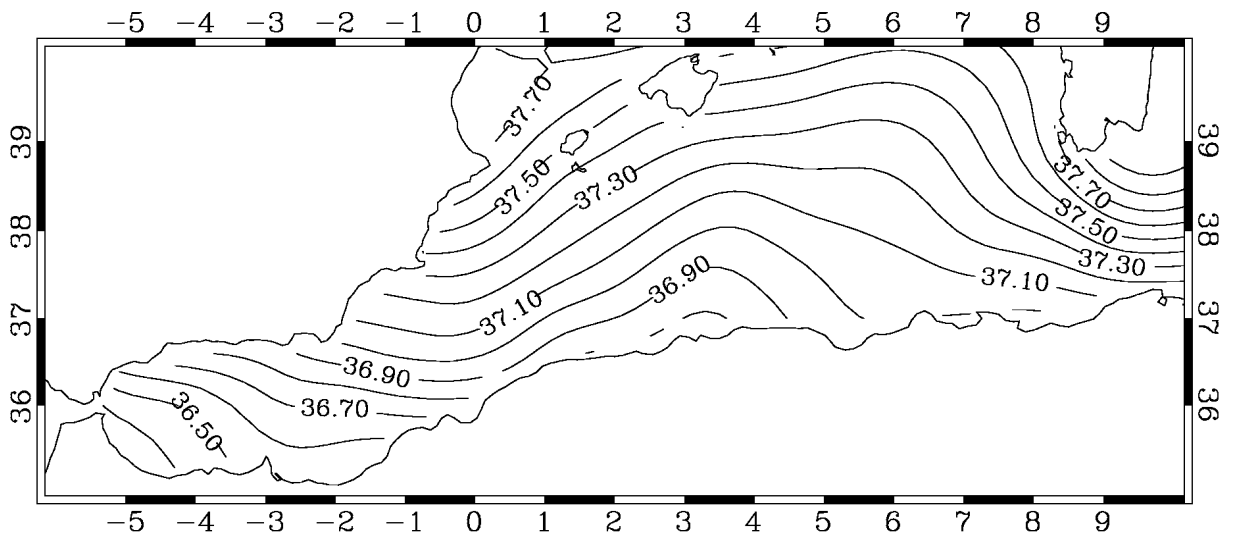


Fig. 8. Climatological distribution of salinity in the area of study at 5 m depth from the MEDATLAS-II data set.

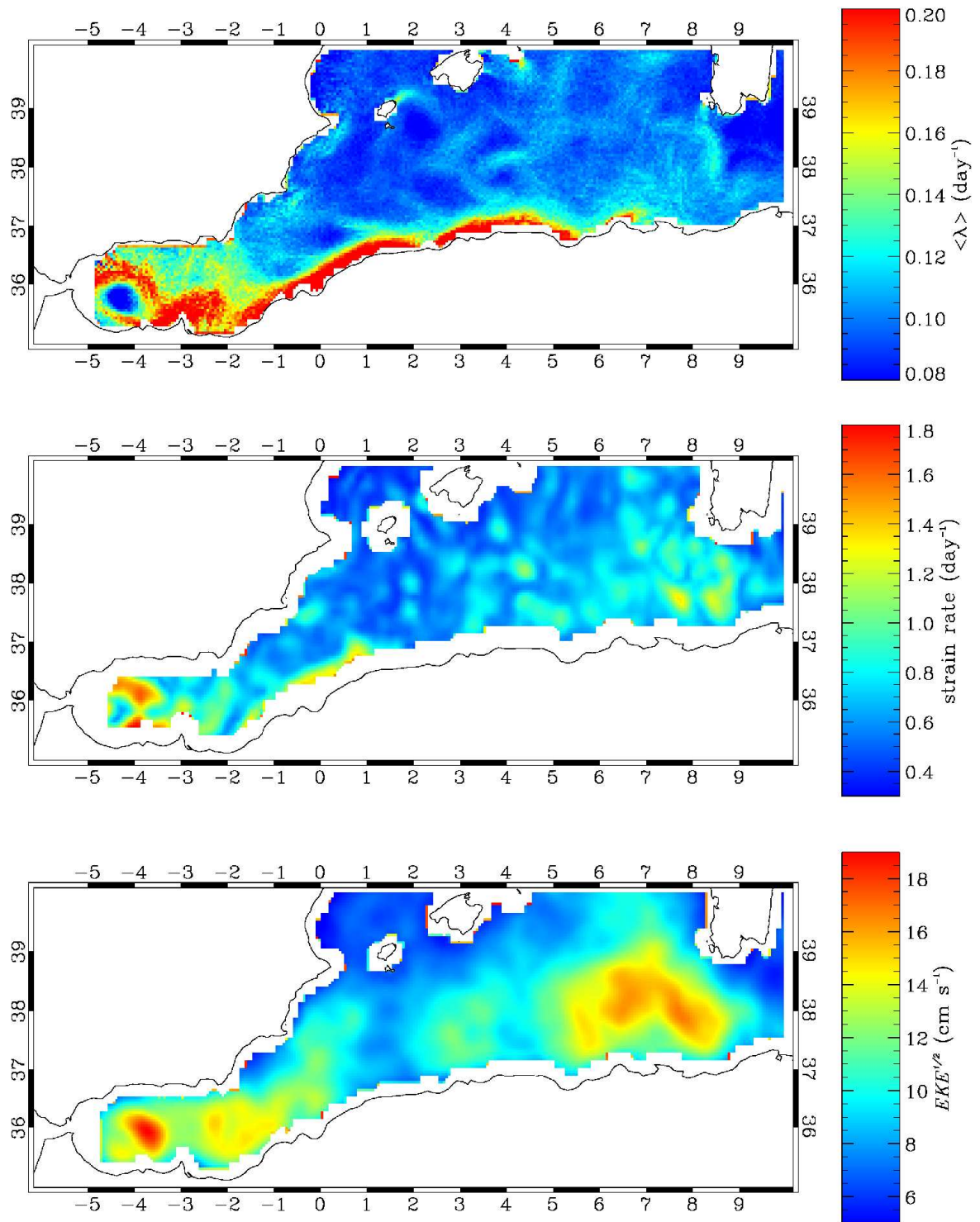


Fig. 9. Time-averaged FSLE, strain rate and eddy kinetic energy (1994-2004).

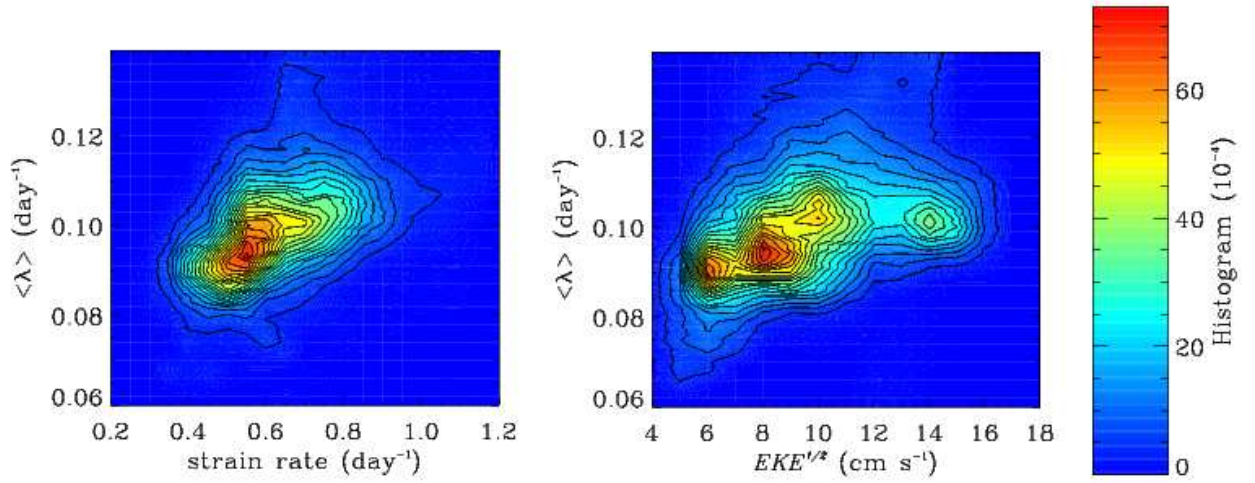


Fig. 10. Joint distributions of Finite-size Lyapunov exponents vs. strain rate values (left), and Finite-size Lyapunov exponents vs. eddy kinetic (right) from the spatial distributions time-averaged over the period 1994-2004.

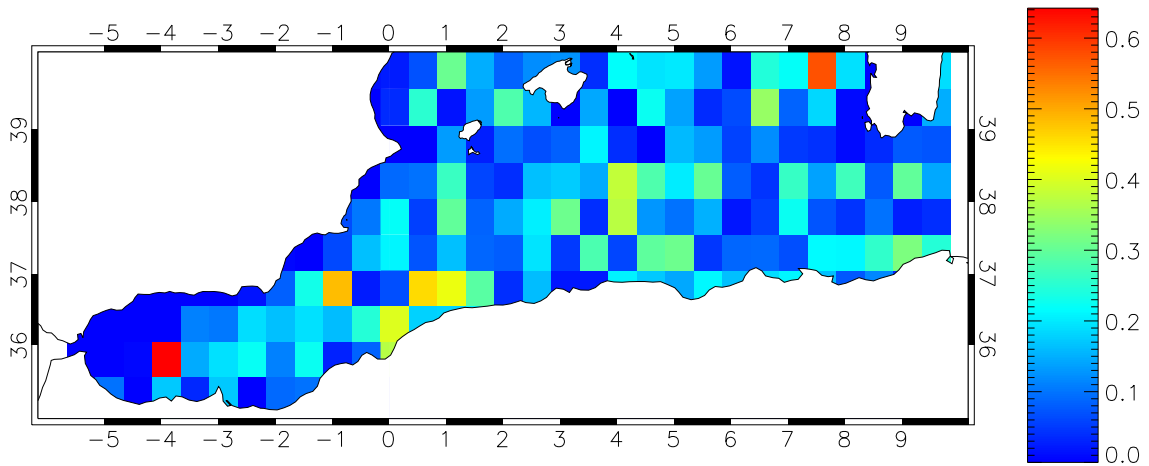


Fig. 11. Calculation of the FSLE for July 9, 2003 with initial separation $\delta_0 = 0.5^\circ$. Compare with Fig. 3 a. At this resolution, Lyapunov exponents cannot be linked to tracer filaments.